Tensile deformation and failure of AlSi10Mg random cellular metamaterials

Laura Salvi, Benjamin Smaniotto, François Hild, M Gabriella Tarantino

Highlights

Tensile deformation and failure of AlSi10Mg random cellular metamaterials

L. Salvi, B. Smaniotto, F. Hild, M.G. Tarantino

- The mechanisms of ductile fracture were revisited using random porous metamaterials
- Structural disorder was found to delay long-wavelength localization
- Void-sheeting was observed with increasing pore aspect ratio
- McClintock's model underestimated void growth data within the failure band

Tensile deformation and failure of AlSi10Mg random cellular metamaterials

L. Salvi[a,1], B. Smaniotto[b], F. Hild[b], M.G. Tarantino[b,*]

[a] *Department of Mechanics, Politecnico di Milano, 20127, Milan, Italy*
[b] *Université Paris-Saclay, CentraleSupélec, ENS Paris-Saclay, CNRS LMPS - Laboratoire de Mécanique Paris-Saclay, 91190 Gif-sur-Yvette, France*

Abstract

Cellular metamaterials are an emerging class of porous materials, in which the topology of the solid is *precisely-engineered* to achieve attractive combinations of properties. This work specifically examines the tensile response of a novel type of cellular metamaterials, in which pores of arbitrary elliptical shape are randomly-dispersed into an aluminum alloy matrix. Their porous mesostructure is generated numerically via a random sequential absorption algorithm, and is fabricated by laser powder bed fusion from AlSi10Mg powders. The results – obtained by means of digital image correlation combined with X-Ray tomography - highlight the advantages offered by a random cellular topology. These are notably a low sensitivity to geometric imperfections (which result inevitably from manufacturing), coupled with the ability to delay long-wavelength strain localization (which is in turn responsible for failure). Structural disorder also leads to highly heterogeneous deformation patterns, which result from the interaction between geometric pores and promote void growth and coalescence during plastic straining. The presence of manufacturing defects, moreover, exacerbates void interaction and in turn promotes early plastic flow localization. Interestingly, experiments reveal that this class of porous solids effectively display features of the ductile fracture of metals, albeit at the mesoscale. For example, *void-sheeting* is observed with increasing pore aspect ratio and is accompanied by large geometric distortions of the voids upon coalescence. Measured data for the pore strains are, moreover, highly scattered and show a departure from McClintock's model predictions for the voids within the fracture band. Collectively, this study highlights the potential offered by random porous metamaterials, which can be harnessed to revisit the

*Corresponding author.
Email address: gabriella.tarantino@universite-paris-saclay.fr (M.G. Tarantino)

complex mechanisms of ductile fracture at the mesoscale.

Keywords:

Ductile fracture, strain localization, void growth and coalescence, cellular metamaterials, digital image correlation (DIC), laser-powder bed fusion (LPBF).

---

1. Introduction

Metallic cellular materials are a class of lightweight materials consisting of a solid metal matrix and air. They contain pores of arbitrary geometry, whose content can be varied to achieve solid relative densities typically between 80% and 0.1%.They can be classified into *open-* and *closed-cell* solids depending on the connectivity of the pores [1]. The former ones are called *metal sponges* and contain pores that are interconnected; the latter ones are designated as *metallic foams* and consist of non-percolating voids, which are separated from each other by portions of solid matrix. In general, open-cell metal sponges are fabricated by investment casting, by replication processing and by sintering; closed-cell metallic foams are instead produced by foaming techniques [1]. In recent years, the rapid progress in manufacturing technologies has enabled the fabrication of metallic cellular structures with intricate, yet *precisely-controlled*, pore features. Architectured materials made of metals, commonly referred to as metallic *metamaterials*, have been the subject of intensive research as they exhibit properties that compare favorably with those of cellular metals produced by conventional manufacturing processes [2, 3]. *Metallic lattices* fabricated by additive manufacturing are a notable example [3, 4].

Metallic metamaterials offer attractive combinations of properties, as they combine optimized architectures with unique features of metals. The latter ones comprise a large range of physical and chemical properties (e.g., strength, ductility, electrical/thermal conductivity) coupled with additional attributes that include recyclability and environmental durability. Currently, metallic metamaterials are among the most attractive lightweight materials for applications in energy and electronics [5], in transport and defense [6] as well as in biomedical engineering and medicine [7]. Examples of their use include energy-absorbing structures [8], biomedical implants and scaffolds [7], heat-exchangers [9] and electrodes [10] among others [3, 11]. To reveal their potential in many engineering applications, a fine understanding of their mechanical behavior is, often, instrumental.

The mechanical properties of architectured materials were examined by Fleck et al. [2], and results relevant to metallic metamaterials are summarized in [11, 3]. The subject now comprises a vast body of theoretical and experimental work that investigates their elastic (e.g., [12, 13, 14]), elastoplastic (e.g. [12, 15, 16, 17, 14, 13, 18, 19]), fracture (e.g., [20, 21, 22, 23, 24, 25]) and fatigue properties (e.g. [26, 27]). Collectively, these studies show that the mechanical performance of metallic metamaterials mainly depends upon the internal mesostructure. Important topological features comprise the pore connectivity (e.g., open or closed) [12], the cell geometry [16] and the void arrangement (e.g., periodic or disordered) [14]. To date, the mechanical properties of metallic metamaterials have been mostly studied under compression; their tensile deformation and failure have been comparatively less examined. The reason for this discrepancy is two-fold. First, they have a high potential as structures that absorb mechanical energy, for which compressive properties are of primary importance. Second, in tension, more than in compression, internal damage is exacerbated leading to a lower macroscopic ductility. At present, experimental studies on the tensile properties of metallic metamaterials are (very) few and remain mostly limited to unit-cell based lattices [14, 28, 24, 22, 17]. Examples include structures fabricated by laser powder bed fusion (LPBF) using steel [24, 17], aluminum- [22] and titanium- [14] alloy powders, as well as low-carbon steel honeycombs fabricated by water-jetting [28]. Collectively, these investigations show that metallic metamaterials have low tensile ductility. Data for this property are highly scattered [24], and display magnitudes that are by far lower than their compressive counterparts [25, 14]. For instance, titanium-based gyroid lattices produced by LPBF typically break at strains less than 10% in tension and greater than 40% in compression [14]. Similar trends are also observed for the flow stress and for the ultimate strength [14, 25].

The knockdown in tensile properties results from internal damage accumulation. The latter in turn has multiple origins. One is associated with the presence of defects (such as, e.g., microporosity [29] and geometric imperfections [13]), which result inevitably from manufacturing and cause severe strain concentrations that eventually initiate the damage process. Another one is the cellular topology, which dictates the deformation mechanisms [16] and consequently affects the rate of damage accumulation. To date, the role of manufacturing defects and topology on the failure mechanisms of metallic metamaterials produced by additive manufacturing has been largely examined under compression (e.g., in [18, 19]). Their

combined effect on tensile failure has been scarcely documented [18]. This is the goal of the present study.

In the following, the tensile response of metallic metamaterials produced by LPBF is studied experimentally. Specifically, the metamaterials of this study contain cylindrical voids randomly-dispersed into an aluminum matrix. Voids have arbitrary elliptical geometry and are algorithmically generated prior to fabrication. Using digital image correlation (DIC) combined with X-Ray computed tomography, the tensile deformation mechanisms of this class of cellular solids are quantified at the mesoscale, and are shown to combine features of the ductile fracture of metals with the defect sensitivity of additively-manufactured cellular materials. The paper is organized as follows. In Section 2, the experimental methods comprising the random porous design, manufacturing and testing are described. The results are presented in Section 3, and give the effective tensile properties alongside the mesoscale deformation fields. The experimental findings are rationalized in Section 4, where the emphasis is put on elucidating the mechanisms of void growth and interaction during plastic straining. Data for the average pore growth rate are compared with the well-known McClintock's micromechanical model [30], and highlight the role of the random porous topology, combined with manufacturing defects, on strain localization.

2. Experiments

This section describes the experimental methods used throughout the study. It begins with the description of the random porous design (Section 2.1) and LPBF manufacturing (Section 2.2). The testing protocol is presented in Section 2.3, while the basics principles of Finite-Element (FE) based DIC (used to measure the kinematic fields during tensile deformation) are recalled in Section 2.4.

2.1. Porous design

Metallic cellular architectures with randomly-dispersed cylindrical pores were designed, fabricated and tested. Their porous structure was generated numerically, prior to fabrication, using a random sequential adsorption (RSA) algorithm [31, 32, 33]. This procedure works by placing (randomly, sequentially and irreversibly) non-overlapping particles in a cell of arbitrary geometry and dimensions (e.g., 2D or 3D); it stops when the target particle content

is reached. Particles can have arbitrary ellipsoidal shape, size and orientation and can be made from any constituent phase (e.g., solid or air), thereby enabling for the design of countless composite architectures [31, 32, 33, 34, 35]. In the present work, the RSA algorithm was used to generate 2D porous geometries with voided particles. More specifically, two types of porous architectures were designed for this study, namely, one consisting of elliptical pores (Figure 1(a)), the other one of circular voids (Figure 1(b)). Both architectures had 20% nominal porosity and contained 200 equisized voids. In particular, the elliptical pores had identical orientation and constant aspect ratio $w = 0.3$ (this parameter designates the ratio of the pore major to the minor axes).

Geometric models of the tested specimens were then created using the 2D RSA-generated porous cells. To build the corresponding 3D models, the open-source software *Gmsh* was used, and the meshes were then extruded out-of-plane prior to fabrication [33, 34]. Two geometries were generated in this study, namely, cubic and dogbone. The first ones had dimensions $12.5 \times 12.5 \times 12.5$ mm^3 and were employed to examine the topological features of the *as-manufactured* cellular architectures by metallographic analyses. The latter ones were designed for mechanical testing. Specifically, dogbone samples had a nominal length of 110 mm and gauge section of 13.5×4 mm^2 (Figure 1(c)). Their porous gauge area comprised two identical porous cells (with dimensions 13.5×12.5 mm^2), whereas the homogeneous heads were 25 mm-wide. Each specimen therefore contained 400 pores (i.e. 200 per cell) that were oriented, in the case of the elliptical pores (Figure 1(a)), with their major axis parallel to the sample longitudinal axis.

The choice of the adopted porous design, comprising two nominally identical porous cells, was made for a two-fold purpose. The first one was to assess the repeatability of the fabrication process and, notably, of the manufacturing defects within the same specimen. The second one was to probe the differences in the deformation behavior between the two porous cells. The latter ones are likely to contain a different distribution/amount of manufacturing defects, as shown by earlier work, e.g., for AlSi10Mg lattice structures produced by LPBF [19]. Last, in the present design (Figure 1(c)), the pores between the two cells were separated by a small, yet noticeable, matrix ligament. The latter extended through the whole specimen thickness and resulted from the cell patterning. As shown in Sections 3.3 and 3.4, this region of the specimens often contained internal defects (in the form of irregular cavities), which resulted

from the fabrication process and promoted strain concentrations.

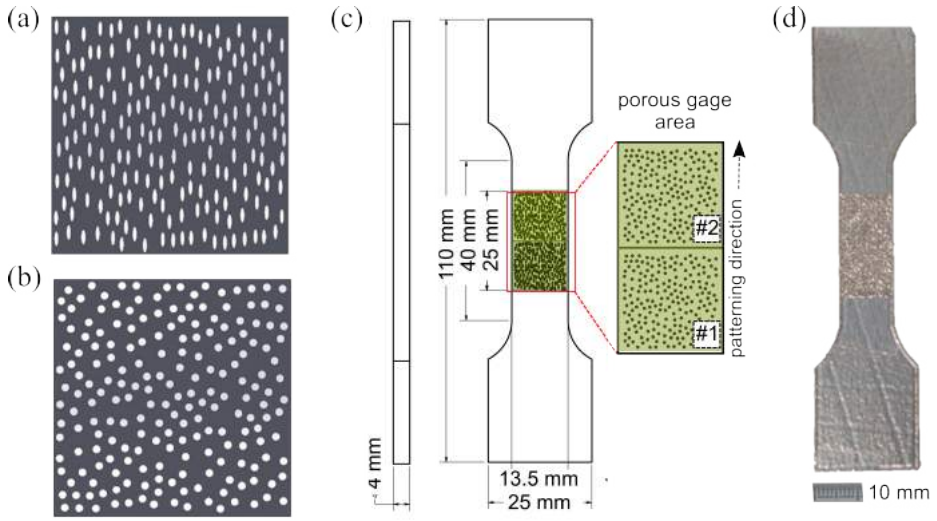

Figure 1: (a,b) Random porous architectures explored in this study. They are generated by means a numerical algorithm, and contain random distributions of equisized (a) elliptical and (b) circular pores at 20% volume fraction. The elliptical pores have identical orientation and constant aspect ratio $w = 0.3$. (c) Geometry of the tensile dogbone specimen comprising two identical porous cells. (d) Optical front-view of the *as-manufactured* tensile specimen.

A total of four specimen geometries were fabricated for this study using different porous realizations; their main characteristics are reported in Table 1. A short-hand designation is used in the form *M20-wY* to distinguish each sample, where M denotes the specimen geometry (C for cubic and D for dogbone), *20* the nominal porosity and Y the pore aspect ratio w. In all specimens, pores had micrometric size with nominal (i.e., *as-designed*) average diameter of 500 μm (Table 1). This parameter corresponds to the average value between the pore major and minor axes, which have both identical values for specimens containing circular voids.

Table 1: Porous specimen specifications

Designation	No of pores	Average pore size	Pore aspect ratio
D20-w1	400	450 μm	1
D20-w03	400	500 μm	0.3
C20-w1	200	450 μm	1
C20-w03	200	500 μm	0.3

2.2. Manufacturing

The porous specimens were manufactured by LPBF (Figure 1(d)) using a SLM HL 125 machine (SLM Solutions GmbH, Germany). It was equipped with a 500-W Yb:YAG laser, whose wavelength and spot diameter were 1070 nm and 70 μm, respectively. A commercial AlSi10Mg powder (TEKNA Advanced Materials Inc, Sherbrook, Canada) was employed for fabrication. It was produced by plasma spherodization and contained, in addition to Al, $\sim$ 10 wt% of Si and $\sim$ 0.25 wt% of Mg. The specifications of its particle size distribution were provided by the manufacturer and are D10 = 20 μm and D90 = 63 μm. The fabrication was performed under argon atmosphere, and the oxygen content was maintained below 1000 ppm during the entire process. Printing was carried out using an incremental scanning strategy, with 67° rotation between two consecutive layers, and a constant powder layer thickness of 30 μm. Since the specimens contained through-thickness cylindrical pores, their building direction was parallel to the longitudinal axis of the pores. Moreover, each sample was produced using two contour passes followed by a hatch (i.e., volume). The selected manufacturing parameters are reported in Table 2.

Table 2: LPBF-process parameters used in this study

	Laser power	Scan speed	Hatch distance	Beam offset[†]
Volume	300 W	400 mm/s	170 μm	
Contour	300 W	1000 mm/s	100 μm	170 μm

[†] it designates the distance between the nominal contour of the part and the center of the laser beam

2.3. Mechanical tests

The porous dogbone specimens D20-w1 and D20-w03 (Table 1) were tested in tension. Prior to the experiments, they were subjected to a standard T6-like heat treatment in order to homogenize the microstructure [36]. It consisted in a solution annealing at 520°C for 1 h followed, in successive order, by water quenching at room temperature, and by artificial aging at 160°C for 6 h. Temperature and interval time recommendations provided in Ref. [36] were adopted. Several studies have shown that the T6-like heat treatment promotes microstructure recrystallization [36, 37], and in turn improves the alloy ductility and fatigue strength [38].

The experiments were conducted under a displacement control mode at a nominal strain rate of $\dot{\epsilon} \leq 10^{-4}$ s^{-1} until sample failure. The experimental setup used in this study is shown in Figure 2. It comprised (i) a uniaxial testing machine equipped with a 100±0.01 kN load cell; (ii) two optical cameras and (iii) an external unit for image acquisition. The two cameras were placed on either side of the specimen to track the deformation of the outer porous surfaces. In the following, they are designated as Cameras F and R (where F stands for front and R for rear, Figure 2). The first one employed a telecentric lens with a resolution $\simeq 25$ μm/px; the latter one was equipped with a standard lens with a resolution of $\simeq 50$ μm/px.

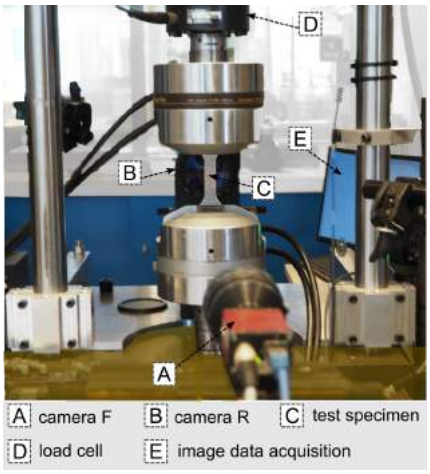

Figure 2: Tensile testing apparatus used in this study. It comprises a uniaxial testing machine equipped with a 100-KN load cell (D) and two optical cameras (A , B) placed on either side of the specimen surface (C). Images from both cameras were collected by means of an external data acquisition system (E) and were used to measure the local deformation fields of the specimen surfaces.

After tensile testing, specimens D20-w1 and D20-w03 were scanned using of a X-Ray tomograph (North Star Imaging X50+). A total of 900 radiographs per scan was collected while rotating the sample between 0 and 360°. An average of 10 images were taken at each rotation step. The X-ray tube was operated at an acceleration voltage of 150 kV using a tungsten transmission target with a 100 μA current. The resolution was $\simeq 18$ μm/voxel. A filtered-back projection algorithm was employed to reconstruct 3D images from the series of acquired radiographs. No filtering was applied.

2.4. Strain measurements by Finite Element-based DIC

Strain was quantified on two opposite surfaces of each dogbone specimen via DIC. Notably, the Green-Lagrange strain fields were computed from the displacement fields, obtained from each correlation process using a Finite Element discretization (Appendix 7). In what follows, the DIC method used throughout the study are briefly recalled.

2.4.1. Digital Image Correlation

The present section summarizes the basic principles of FE-based DIC. The correlation technique was used herein to measure displacement fields $\mathbf{u}(\mathbf{x})$ extracted from images acquired during the two tests. This operation is possible thanks to the application of gray level conservation

$$f(\mathbf{x}) = g(\mathbf{x} + \mathbf{u}(\mathbf{x})) \tag{1}$$

between two images g and f, corresponding respectively to the deformed and reference configurations. The correlation procedure aims at minimizing the gray level residuals $\varphi(\mathbf{x})$ over the chosen Region Of Interest (ROI) with respect to the nodal displacements gathered in the column vector $\{\mathbf{u}\}$

$$\varphi(\mathbf{x}) = f(\mathbf{x}) - g(\mathbf{x} + \mathbf{u}(\mathbf{x}, \{\mathbf{u}\})). \tag{2}$$

Thus, the aim of the DIC code is to iteratively minimize the sum of squared differences

$$\Phi_c^2 = \sum_{ROI} \varphi_c^2(\mathbf{x}) \tag{3}$$

with respect to the unknown degrees of freedom $\{\mathbf{u}\}$ of the parameterized displacement fields. Since a FE approach was adopted, the displacement field is written as

$$\mathbf{u}(\mathbf{x}) = \sum_n u_n \boldsymbol{\psi}_n(\mathbf{x}), \tag{4}$$

where u_n denote the unknown nodal displacements, and $\boldsymbol{\psi}_n$ the corresponding shape functions. It is worth noting that the actual pore positions were recovered through backtracking (see Appendix 7).

In global approaches, the continuity of displacements is assumed *a priori*, which corresponds to a first regularization. To speed-up convergence to the solution, the displacement field can be further regularized by means of a penalty term that acts as a low-pass filter [39].

Regularization may apply on total or incremental displacements. The method adopted in the current work considered incremental regularization [40], from one step of the correlation analyses to the next, which constitutes a milder approach adapted for plasticity. The penalization is based on the equilibrium gap [41], which states that for force-free nodes the corresponding nodal force should cancel out

$$\Phi_m^2(\{\partial \mathbf{u}\}) = \{\partial \mathbf{u}\}^\top [\mathbf{K}]^\top [\mathbf{K}] \{\partial \mathbf{u}\}, \tag{5}$$

where $\{\partial \mathbf{u}\}$ is the column vector gathering all nodal displacement increments between image n and $n+1$, $[\mathbf{K}]$ the rectangular stiffness matrix associated with the force-free nodes. The total cost function then becomes

$$\Phi_t^2 = \Phi_c^2 + \omega \Phi_m^2, \tag{6}$$

where the weight ω is selected by the user, and is proportional to a (regularization) length ℓ_{reg} raised to the power 4 [39]. In the present work, the DIC technique was implemented within Matlab and C++ kernels developed at our laboratory [42].

2.4.2. Regularization length and uncertainty

When starting any DIC analysis, the ROI is to be defined, meshed, and a regularization length must be selected in order to reduce uncertainties and help the convergence of the correlation algorithm. A value that does not filter out too many useful details is to be chosen. When performing the analyses, the uncertainty estimate was used to evaluate the accuracy of the measurements. In order to evaluate the measurement uncertainties, prior to starting the experiments *per se*, about 100 pictures were acquired for the unloaded specimen. In the present case, only the standard strain uncertainties are reported. They were assessed for each camera of each tested specimen. Table 3 shows that for the selected regularization lengths, the standard strain uncertainties were all less than $3 \cdot 10^{-4}$.

Table 3: Uncertainty quantification of longitudinal strain (E_{yy}) fields. In addition to the standard uncertainties, the regularization lengths (ℓ_{reg}) and mean element sizes (ℓ) are reported for each considered case

	ℓ_{reg} Camera F	Std(E_{yy}) Camera F	ℓ Camera F	ℓ_{reg} Camera R	Std(E_{yy}) Camera R	ℓ Camera R
D20-w1	30 px	$3.1 \cdot 10^{-4}$	3.6 px	40 px	$1.9 \cdot 10^{-4}$	3.2 px
D20-w03	30 px	$1.2 \cdot 10^{-4}$	3.7 px	40 px	$2.9 \cdot 10^{-4}$	4.0 px

A regularization length of 30 px was adopted for Camera F acquisitions, which was characterized by a lower acquisition noise level; whereas a value of 40 px was adopted for Camera R. Beyond random factors such as the applied speckle pattern and stroke fluctuations (the hydraulic testing machine was on and the feedback loop was active), the uncertainty was also impacted by the camera, element size and regularization length. In this particular case, higher values of uncertainty around the porous region were due to smaller element sizes needed to describe the pore geometry. Despite these various sources, the standard uncertainty levels remained rather small in comparison to the strain levels that developed in the four analyses.

As reported in Table 3, the element sizes ℓ adopted for the porous specimens studied via DIC was of the order of 3-4 px. This very fine discretization was needed in order to capture local strain distributions around pores and required the use of mechanical regularization.

3. Results

This section reports the major experimental results of this study and includes both microstructural observations (Section 3.1) and data measured during mechanical tests (Sections 3.2 to 3.4). The macroscopic tensile response of the AlSi10Mg random cellular metamaterials is presented in Section 3.2, while the fracture surfaces are examined in Section 3.3. The latter also reports a thorough investigation, carried out by means of X-ray computed tomography, of the matrix internal defects resulting from LPBF manufacturing. The mesoscale strain patterns measured by FE-based DIC, using meshes consistent with the pore topology, are displayed in Section 3.4.

3.1. LPBF-manufactured cellular topologies

Optical microscopy was used to examine the topological features of the as-fabricated cubic porous samples C20-w1 and C20-w03 (Table 1). Micrographs are presented in Figure 3 and are contrasted with the corresponding geometrical models.

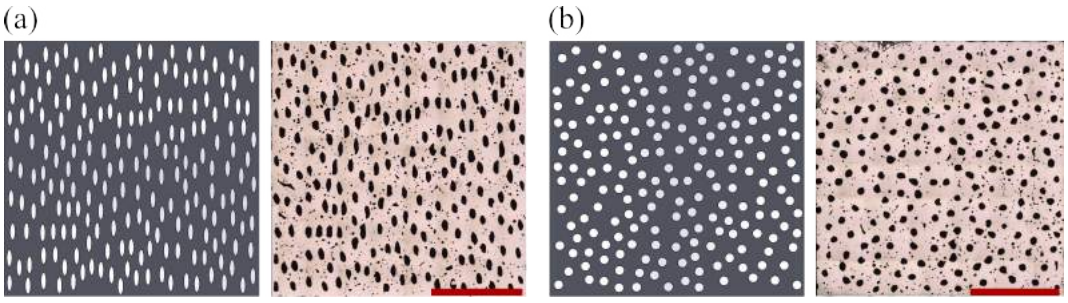

Figure 3: Optical micrographs of the AlSi10Mg cubic porous samples (a) C20-w03 and (b) C20-w1 containing respectively a random packing of elliptical and circular pores. The porous specimen specifications are given in Table 1. For both porous architectures, experimental micrographs are contrasted with the corresponding geometrical model. Scale bar: 3 mm.

For both porous architectures, the presence of manufacturing defects, such as matrix internal porosity and geometric imperfections, was observed. Internal matrix porosity occurred in the form of small and irregular voids within the matrix. Topological defects were instead distinguished by morphological mismatches between the as-designed and the as-manufactured pore geometry. Notably, the printed pores were found to have non-uniform ellipticity, lower roundness and more irregular size than their nominal (*defect-free*) counterparts. For example, Figure 3(a,b) reveals that geometric voids were smaller near the cell edges and had a more polyhedral shape, when they are closely-spaced.

3.2. Stress-strain response

The tensile response of AlSi10Mg dogbone samples D20-w03 and D20-w1 is reported in Figure 4. For both pore geometries, data for the macroscopic engineering stress are plotted against the longitudinal strain $\langle E_{yy} \rangle$. This last quantity is computed by means of FE-based DIC (Section 2.4) and corresponds, unless specified otherwise, to the average axial strain measured over the entire porous gauge area (Figure 1(c)). In the interest of comparison, measurements from both cameras are reported using different line styles. Collectively, data in

Figure 4 show similar trends. In particular, three distinct stages of deformation corresponding to (i) initial elasticity, (ii) strain hardening up to the peak stress and (iii) final strain softening, are discerned from the stress-strain curves. For both porous architectures, the macroscopic tensile curve exhibits a departure from linearity at a strain level of about 0.1% (this value is denoted by the dotted line [a] in Figures 4(a,b)). Upon yielding, the response strain-hardens and the tensile flow stress increases continuously up to the peak load. The measured flow stress is notably higher for specimens D20-w03 (containing elliptical voids), and reaches its maximum value at a strain between 0.6 and 0.7% for both specimen geometries (Figures 4(a,b)). Beyond the peak stress, the tensile response of both samples is characterized by the occurrence of repeated stress drops; strain softening continues until final fracture of the sample. Overall, the results are also fairly reproducible. For each specimen geometry, the difference between the average strain measured by the two cameras remains very small until the attainment of the peak stress, and only increases slightly (past this point) as a result of damage softening. The highest strain difference is of the order of $\approx$ 0.3%, and is measured for specimen D20-w03 (as seen by comparing, e.g., curves in Figures 4(a,b) past 1% strain denoted with the dotted line [e]).

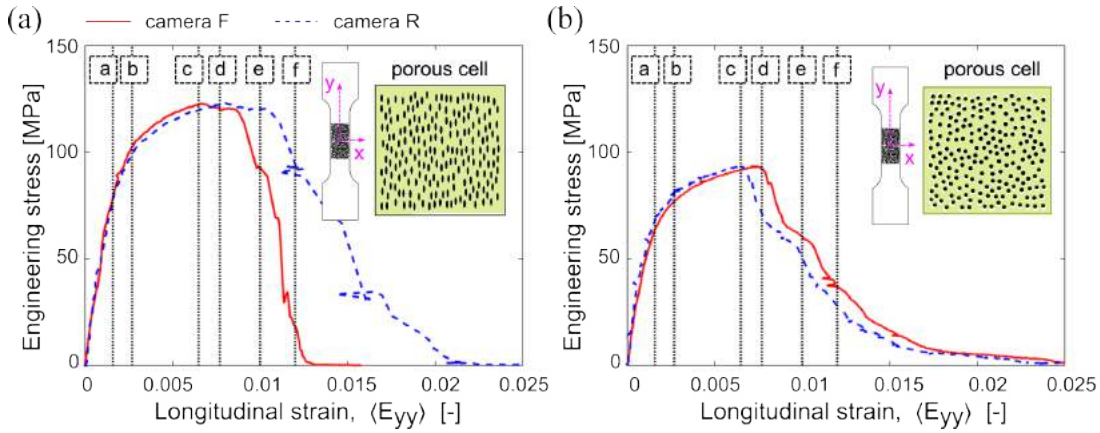

Figure 4: Experimental tensile stress-strain curves for the AlSi10Mg porous samples (a) D20-w03 and (b) D20-w1. The specimens specifications are given in Table 1, whereas their porous cell is shown in the inset of each figure. For both samples, the macroscopic stress is plotted against the average longitudinal strain $\langle E_{yy} \rangle$ computed over the entire porous gauge area by means of FE-based DIC. Strain measurements from images collected by the two cameras are denoted with different line colors. Note that Camera F of sample D20-w03 could capture only one porous cell.

3.3. Post-mortem X-Ray Tomography

Tomographic sections from reconstructed volumes of the dogbone samples, scanned after mechanical testing, are presented in Figures 5(a,b). In the interest of comparison, images corresponding to the outer and mid sections are reported for each porous geometry. As seen, the fracture surfaces of the two mesoporous specimens display distinct characteristics. In sample D20-w1 containing circular pores (Figure 5(a)), fracture occurred in the lower porous cell and exhibited a band-like crack path. The latter was inclined with respect to the loading axis and traversed a large number of voids across the specimen's width. By contrast, the fracture path displayed by sample D20-w03 with unidirectional elliptical voids (Figure 5(b)) was more irregular, and involved an extended region of the specimen comprised between the two porous cells. Failure, moreover, encompassed only a few voids (Figure 5(b)). Collectively, the observed fracture features are reproducible across the scanned volumes and no significant differences can be discerned among the three tomographic sections, for each specimen geometry.

Tomography also reveals the presence of matrix internal defects, such as small pores and irregular cavities. To examine their morphological characteristics, a representative portion of the matrix volume within sample D20-w03 was analyzed using the *Avizo* software. This is highlighted in Figure 5(b) and consisted of 794 x 214 x 236 voxels^3 for a total volume of $\sim 164.25 mm^3$. Results of the tomographic reconstructions are presented in Figures 5(c,d), whereby the Al-alloy matrix is shown with full transparency. To improve the presentation, geometrical pores are depicted with blue color. Tomographic images show two populations of matrix defects, whose total volume fraction was $\approx 2.4\%$. This last quantity was computed with respect to the total volume of the region highlighted in Figure 5(b), using the *Avizo* software. Matrix defects can be discriminated on account of their morphology, and are represented with red and yellow colors (Figures 5(c,d)). The first ones have smaller sizes and display a bubble-like shape. The second ones have larger and more irregular shape (see, e.g., defects denoted as #1 and #2).

The findings of Figures 5(c,d) corroborate the metallographic observations reported in Figures 3(a,b) (for different realizations of the same random topologies), and also indicate that defects shown here result from LPBF. Notably, their distribution and morphology depend on the adopted laser strategy. Figure 5(c) illustrates this point. It shows that bubble-like

defects formed in the matrix ligament surrounding the geometric pores, and lied along the laser *contour* trajectories.

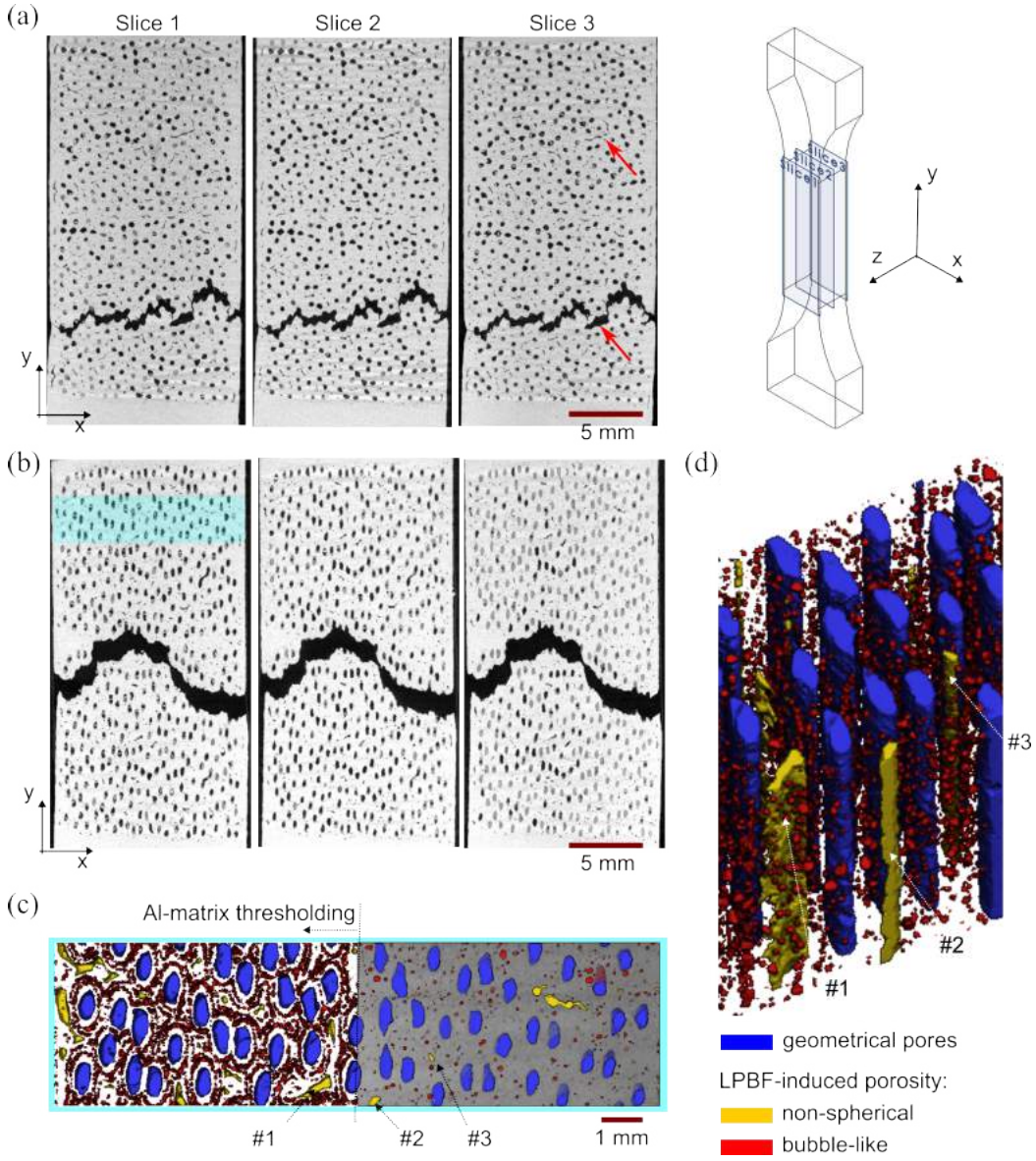

Figure 5: Tomographic sections of the reconstructed internal volume of specimens (a) D20-w1 and (b) D20-w03. They were scanned after mechanical testing. Representative examples of large matrix defects occurring at identical locations within the specimen are indicated with red arrows in sub-figure (a). (c) Front and (d) isometric view of a selected portion of the reconstructed volume for specimen D20-w03, highlighted with light-blue color in sub-figure (b) and showing the presence of process-induced porosity within the matrix. To improve the presentation, the Al-alloy matrix is shown with full transparency using the *Avizo* software.

Figure 5(d), instead, reveals that irregular defects (depicted with yellow color) extended consistently throughout the sample thickness, which in turn corresponds to the part building direction. This observation is consistent with the tomographic section reconstructions reported in Figures 5(a,b). The latter ones also show that defects of this type occurred at about the same location within the specimen, irrespective of its cellular topology. An example is shown in Figure 5(a)-Slice 3 and is highlighted with red arrows. Figures 5(c,d) also indicate that bubble-like defects are present in the largest amount within the matrix of the analyzed sub-volume. To quantify their morphological characteristics, measurements of the volume and shape factor (sphericity) were obtained, for each reconstructed pore defect, using built-in *Avizo* functions. Their statistical distribution is reported in Figure 6. Figure 6(a) displays the volume distribution computed from data obtained via the *Volume3D* function, and shows that most of the bubble-like defects did not exceed 10^{-5} mm^3 in volume. Pores whose volume is greater than 10^{-3} mm^3 are rare (see the inset in Figure 6(a)). The distribution in Figure 6(b) also indicates that most of the bubble-like pores are characterized by a sphericity factor close to unity. This last quantity was obtained via the *ShapeVA3D* function (where ShapeVA3D $= A^3/(36\pi V^2)$ was computed, for each pore, from its volume V and area A), and has a value equal to unity when the pore is a perfect sphere. Representative examples of the 3D pore shapes associated with an increasing value of the sphericity factor, in parts built by LPBF, are given in Figure 9 in Ref. [43]. Collectively, the data of Figure 6(b) corroborate the observations in Figures 5(c,d) showing that bubble-like defects were mainly of spherical shape. To quantify their size, the pore equivalent diameter D_{eq} was computed for all defects with sphericity varying between 0.8 and 1.2 from the reconstructed volume (where the latter was assumed to be spherical). Measurements of mean equivalent diameter, at distinct sphericity intervals, are reported together with their standard deviations in the inset of Figure 6(b), and display values ranging from 40 µm to 80 µm.

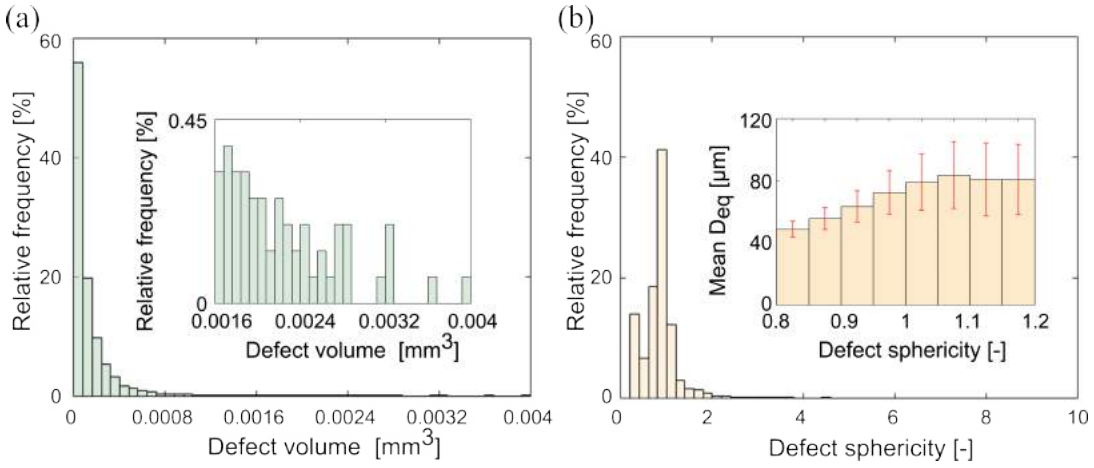

Figure 6: (a) Volume and (b) sphericity distributions of the bubble-like defects within the sub-volume highlighted with light blue color in Figure 5(b). The geometrical characteristics were extracted from the tomographic volume reconstructions using *Avizo* software. To improve the presentation, the relative frequency of the pore defects with volume larger than $1.6 \cdot 10^{-3}$ is shown in the inset of sub-figure (a) using a magnified scale. Likewise, data for the mean equivalent diameter D_{eq} are reported, together with their standard deviations, in the inset of (b) for all defects with a sphericity varying between 0.8 and 1.2. For each pore, D_{eq} was computed from its reconstructed spherical volume.

3.4. Mesoscale strain maps

The local strain fields could be computed by means of FE-based DIC (Section 2.4). For both porous specimens D20-w03 and D20-w1, the axial strain fields are presented in Figures 7 and 8, respectively. The mesoscale strain maps were computed from images collected by the two cameras and are reported for discrete instants of the deformation history. They were selected from the measured stress-strain curves, and correspond to the macroscopic strain levels $\langle E_{yy} \rangle$ denoted with dotted lines in Figures 4(a,b). Results show that:

- upon departure from elasticity, strains have inhomogeneous distribution (Figures 7(a) and 8(a)). When $\langle E_{yy} \rangle \approx 0.15\%$, areas of increased strain levels are observed across the porous surface of both tested specimens, and are uniformly distributed within the gauge area;

- upon strain hardening, distinct strain concentration bands start appearing in both porous specimens (Figures 7(b) and 8(b)). They have short lengths, encompassing groups of few closely-spaced pores, and widths larger than one pore-diameter. Inter-

estingly, the short bands occur at different locations in both specimens and display a symmetric pattern in sample D20-w1 containing circular voids (Figure 8(b));

- near the peak stress, the existing short bands continue to accumulate strains and new ones form with further plastic flow (Figures 7(c,d) and 8(c,d). The interactions between pores become evident and occur, in most cases, within short bands inclined with respect to the loading axis in both tested specimens;

- upon strain softening, a change in the deformation patterns is observed for both porous specimens. Some of the short bands become inactive and the whole deformation concentrates around the fractured zone (Figures 7(e,f) and 8(e,f). Consistent agreement is found between the strain patterns of Figures 7(f) and 8(f)) and the fracture paths displayed in Figures 5(a,b).

The results from the two cameras are also similar, thereby indicating that the deformation was pretty uniform along the sample thickness. This was expected given the specimen geometry, which has extruded porous sections along the building direction. The slight difference between the strain maps, measured with the two cameras, may be rationalized by consideration of their different optical resolution. The latter was higher for camera F equipped with a telecentric lens (Section 2), and allowed the deformation features to be more finely captured. Examples are given in Figures 8(a) and 7(b), whereby zones of strain concentration around large matrix defects could be measured with camera F images and benchmarked against tomographic scans for Slice 1 in Figures 5(a) and 5(b), respectively. Interestingly, the strain maps also show that the strains concentrate in regions of the matrix ligament between the two porous cells (Figures 8(c) and 7(c) obtained with camera F), where irregular pore defects resulted from the LPBF contour strategy (Figure 5(a)). This finding is consistent with the results of earlier work on AlSi10Mg lattice structures produced by LPBF [19], where large irregural pores were observed in the matrix region connecting the elemental struts. Figure 8 also proves that, even though the two porous cells were nominally identical, the corresponding strain patterns became different very early on with increasing macroscopic strain. It is believed that such differences were due to the manufacturing defects present within the matrix of the two cells, Figure 5(a).

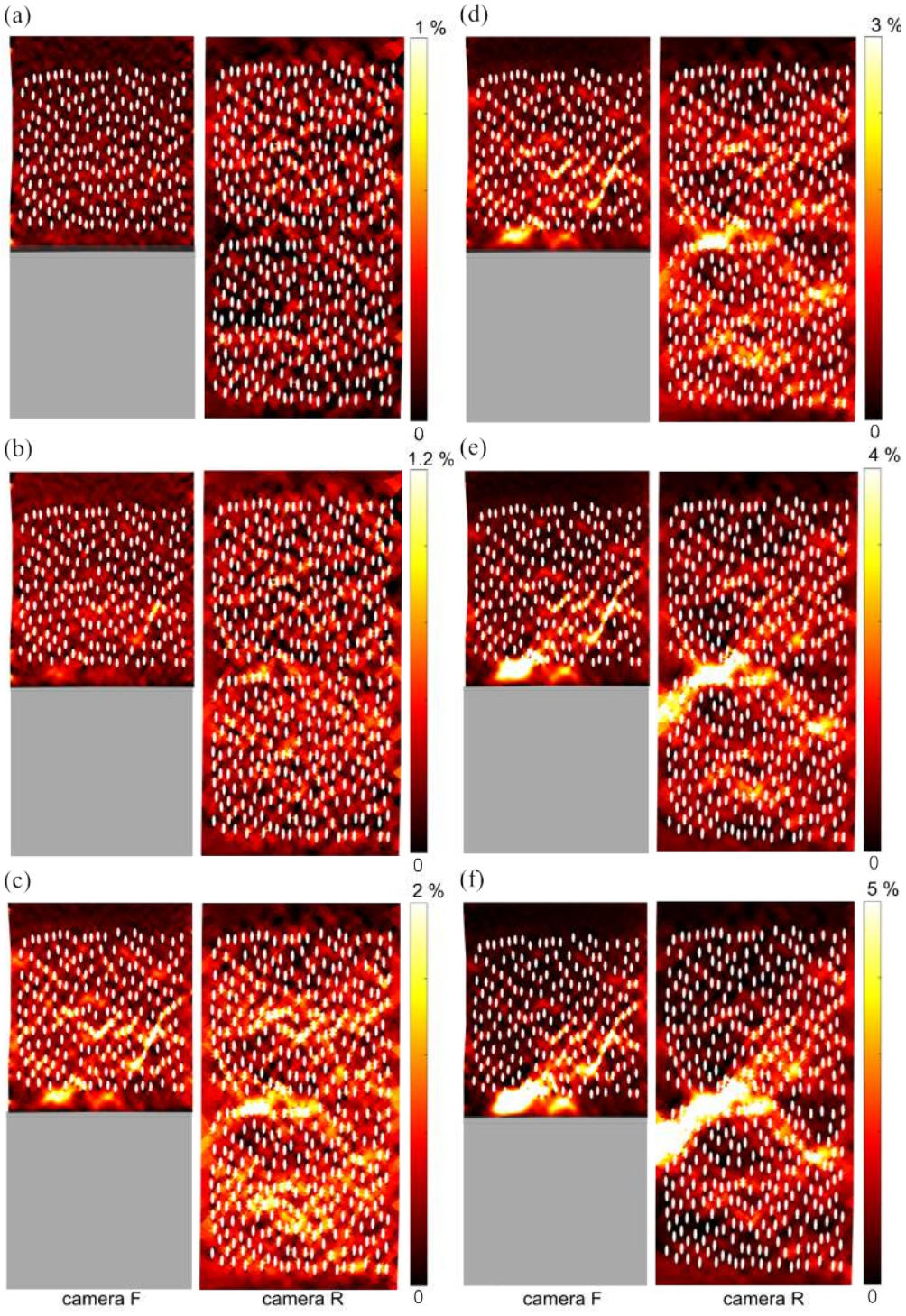

Figure 7: Local axial strain maps for specimen D20-w03 at discrete points of the deformation history. The macroscopic longitudinal strain $\langle E_{yy} \rangle$ is equal to (a) 0.16%, (b) 0.27%, (c) 0.65%, (d) 0.77%, (e) 1% and (f) 1.2%. These levels are depicted with dotted lines in Figure 4(a). The strain fields were computed by means of FE-based DIC using images collected simultaneously by both cameras. Note that since Camera F of sample D20-w03 could capture only one porous cell, the corresponding strain map is reported for the upper cell.

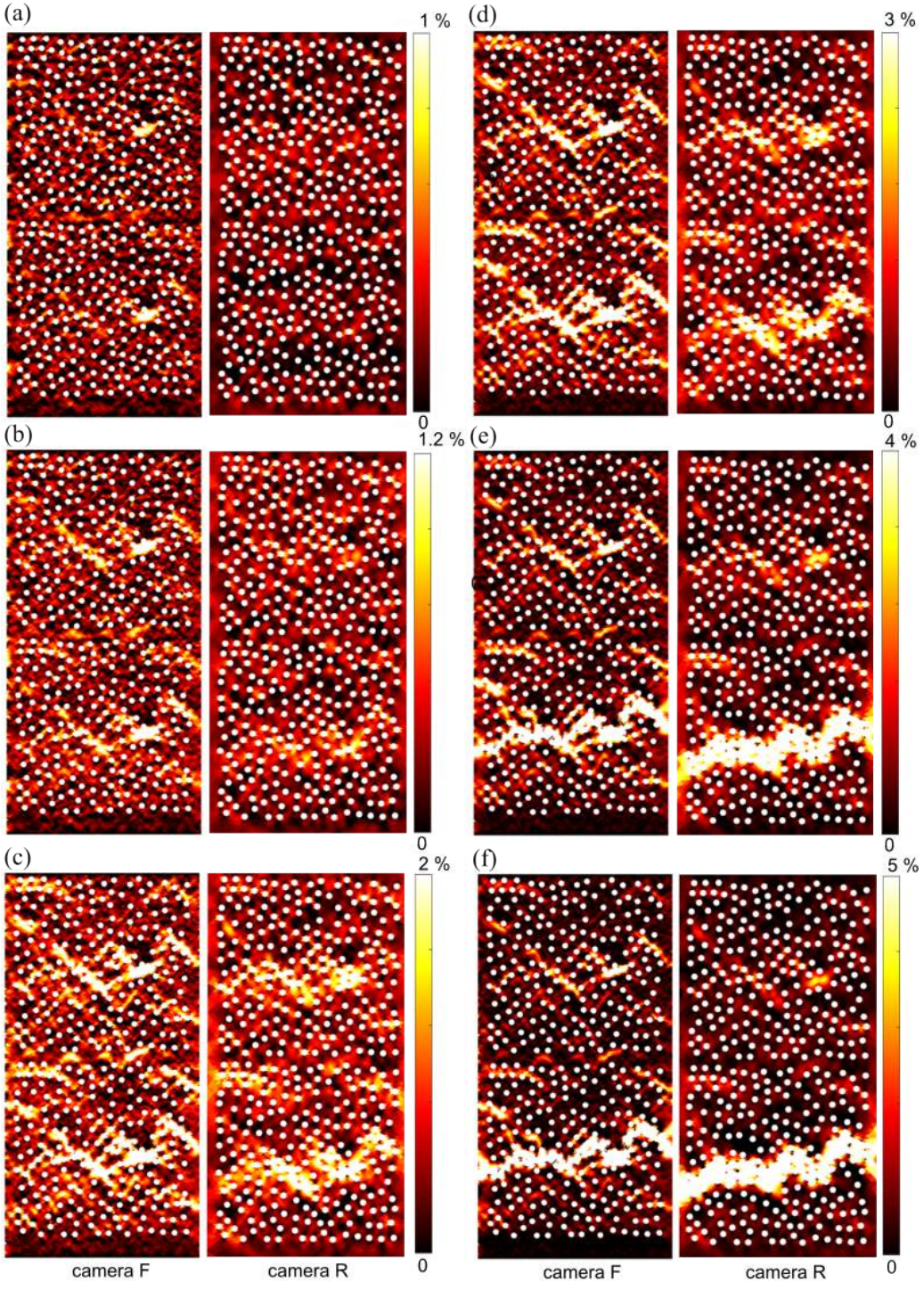

Figure 8: Local axial strain maps for specimen D20-w1 at discrete points of the deformation history. The macroscopic longitudinal strain $\langle E_{yy} \rangle$ is equal to (a) 0.16%, (b) 0.27%, (c) 0.65%, (d) 0.77%, (e) 1% and (f) 1.2%. These levels are depicted with dotted lines in Figure 4(b). The strain fields were computed by means of FE-based DIC using images collected simultaneously by both cameras.

4. Discussion

The main findings of this work are discussed hereafter. First, the effective tensile properties of the AlSi10Mg random cellular metamaterials are summarized in Section 4.1, and are rationalized on account of the cellular topology combined with the presence of manufacturing defects (Section 4.2). The mechanisms of internal damage accumulation are then examined in Section 4.3, and are quantified using DIC data for the pore true strains. Measurements of the average growth rate are also compared with predictions of the McClintock's micromechanical model (Section 4.4), and the main implications for models of ductile fracture are discussed.

4.1. Tensile properties

The random cellular architectures of this work have low elongations to failure despite the inherent ductility of the alloy they are made from (Figure 4). Their tensile properties could be computed from data in Figure 4 and are summarized in Table 4. In data presented herein, the Young's modulus along the longitudinal direction, i.e. E, was measured through linear-regression of the elastic segment of the tensile stress–strain curve, and is reported together with the R^2 coefficient. The yield stress $\sigma_{0.1\%}$ was computed at 0.1% offset strain, whereas the ultimate tensile strength σ_{UTS} corresponds to the peak stress in the tensile response. The elongation at the maximum load is denoted as ϵ_{UTS}. For each specimen tested, data for E, $\sigma_{0.1\%}$ and ϵ_{UTS} were computed using strain measurements from each camera, and are reported together with their average value. Measurements of σ_{UTS} are, instead, independent of the camera sensor. In the interest of comparison, the tensile properties of the AlSi10Mg matrix are also given in Table 4. They were measured in a separate set of experiments on heat-treated bulk samples (produced and tested as described in Section 2), and are consistent with data from literature [44, 36, 38].

Collectively, the results in Table 4 show that the two cellular architectures have similar elastic stiffness but distinct plastic properties. For both porous specimens, the values of the Young's modulus E differ by less than 8% and are slightly higher for sample D20-w03 consisting of elliptical voids. The yield stress $\sigma_{0.1\%}$ and ultimate tensile strength σ_{UTS}, instead, have magnitudes that are up to 40% lower for specimen D20-w1 containing circular pores. Since both samples have equal relative density and contain likely the same amount of internal matrix porosity, the measurements in Table 4 indicate that the pore shape exerts no significant

Table 4: Tensile properties of the AlSi10Mg random cellular architectures of this study and corresponding values measured for the bulk alloy matrix in the same metallurgical state.

		E [GPa]	$\sigma_{y0.1\%}$ [MPa]	σ_{UTS} [MPa]	ϵ_{UTS} [%]
D20-w1	Camera F	38 ($R^2 = 0.988$)	78.6		0.73
	Camera R	39.7 ($R^2 = 0.92$)	82.8		0.65
	average	38.8 ± 0.8	80.7 ± 2.1	93.3	0.69 ± 0.06
D20-w03	Camera F	40.2 ($R^2 = 0.97$)	112.9		0.61
	Camera R	43 ($R^2 = 0.964$)	112		0.72
	average	41.6 ± 1.4	112.4 ± 0.4	122.8	0.67 ± 0.07
AlSi10Mg matrix	Camera F	72.6 ($R^2 = 0.991$)	122.6		14.8
	Camera R	65.9 ($R^2 = 0.883$)	128.6		15.2
	average	69.2 ± 4.7	125.6 ± 10	204.6	15 ± 0.5

influence during elastic deformation. This agrees well with what reported for other random media, containing either solid [45] or voided particles [46]. Conversely, the effect of the void shape becomes more important upon plastic straining in agreement with prior work [47]. In particular, the observed tendency for the tensile strength to decrease as the aspect ratio w increases (compare values of σ_{UTS} for samples D20-w1 and D20-w03 in Table 4) is consistent with trends observed in porous metals produced by unidirectional solidification [48]. These materials have similar cellular topologies and display values of σ_{UTS} that scale as ρ^{1+2w}, where ρ is the relative density (see Equation (14) in Ref. [48]).

Equally important, data in Table 4 indicate that the measured ϵ_{UTS} are of the order of $\sim 0.7\%$ and thus have levels which are one order of magnitude lower than for the bulk alloy. These observations are consistent with what reported for most conventional Al-based foams loaded in tension [49, 50, 51, 52], which typically fractured at strains below a few percents. Prior work also shows that data for the tensile ductility of metallic random foams are highly scattered (see, e.g., Figure 1 of Ref. [53]) and reflect a maximized influence of internal damage accumulation on tensile deformation. For example, San Marchi et al. [51] investigated the tensile response of replicated pure Al and Al-12Si foams at equal relative density, and found that failure strains never exceeded a few percents even for foams made from a very ductile metal (i.e., pure Al). Moreover, measured elongations-to-failure were up to

seven times lower for the Al-12Si foam containing brittle Si phases. Collectively, the findings of this study highlighted the role of internal damage on the low tensile ductility exhibited by metallic cellular materials and were also corroborated by several numerical studies by Mangipudi et al. [54, 55].

The cellular materials produced for this study were made of peak-aged AlSi10Mg alloy and thus contained nearly 10% of Si, typically in the form of globular particles with sizes of a few µm [36, 44, 37]. In bulk form, the alloy exhibits a highly ductile behavior that results from the nucleation and coalescence of microscopic voids (see Refs. [37, 36] and data in Table 4), and is distinguished by the presence of equiaxed dimples observed across the fractured surface. Prior work reported that the average size of the dimples depended on the solution treatment temperature, and reached 5 µm when the alloy was peak-aged above 500°C [37]. Similar features were observed across the fracture surfaces of the broken sample D20-w03 (Figures 9(a,b)), which showed the presence of equiaxed dimples within the matrix (Figure 9(c)). The SEM fractography also revealed that the dimples had a size of a few micrometers (in agreement with earlier work [37]), and were one order of magnitude smaller than the spherical pore defects produced during LPBF fabrication (Figure 6(b)). The latter ones (highlighted with dashed yellow circles in Figure 9(b)) exhibited morphological features that are in quantitative agreement with the tomographic observations reported in Section 3.3. Figure 9(a,b) also shows the presence of unmolten AlSi10Mg powder within the geometric pores. This last observation is common in parts produced by LPBF, and in turn explains why identical pores have different X-Ray attenuation across the thickness of the reconstructed specimen volume (Figures 5(a,b)).

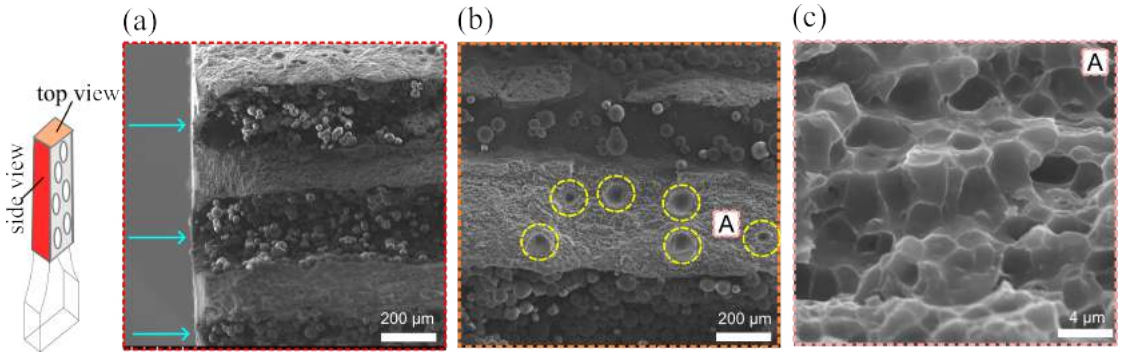

Figure 9: SEM micrographs of the fractured surfaces of sample D20-w03 containing elliptical pores. (a) Side and (b) top views, whereby the through-thickness geometric pores and the matrix internal defects are indicated with cyan arrows and dashed yellow circles in sub-figures (a) and (b), respectively. (c) Close-up view of the matrix region, denoted by A in sub-figure (b), revealing the presence of equiaxed dimples with size of a few micrometers.

The presence of dimples in the matrix ligament between geometric pores (Figure 9(c)) also confirms that brittle fracture of the Si phase was not the dominant cause of internal damage accumulation in the present cellular metamaterials. Another reason for their reduced ductility must exist. This observation points to a geometric cause such as the cellular topology combined with the presence of manufacturing defects. The latter ones resulted from the LPBF process (Figures 3 and 5), and are known to exacerbate the mechanisms by which damage accumulates during plastic deformation [56, 57, 19, 18, 29].

4.2. LPBF-induced defects

The random cellular architectures of this work contained a non-negligible number of manufacturing defects, which occurred either as geometric imperfections or as matrix internal porosity (Figures 3,5). Their classification is given in Section 3.1 together with the description of their morphological characteristics. Both types of defects are known to result from the laser scanning strategy and may have a detrimental effect on the mechanical properties [56, 57, 19, 18, 29, 34]. Topological defects were not quantified in this study but were examined in Ref. [34], for similar porous structures fabricated using a large set of processing parameters and different metallic powders. Internal matrix porosity was instead analyzed using X-Ray tomography and was found to be of two types (i.e. pore- or crack-like, see Figure 5). Pores and cracks are commonly observed within the matrix of parts fabricated

by LPBF [29, 44], and factors governing their formation are well understood also for structures made of AlSi10Mg powders [44, 58]. Specifically, near-spherical pores result either from trapped gas bubbles, during solidification of the base metal, or from the keyhole phenomenon (which is in turn caused by the instability of the melting pool). Crack-like defects, also called *lack-of-fusion* defects, are due either to a low energy density or to a poor overlap of the melt pools. In the present study, the incomplete overlap between adjacent contour and hatch tracks is likely the origin of the lack-of-fusion defects. This hypothesis is corroborated by several observations. First, defects of this type (depicted with yellow color in Figure 5(c)) typically appear within regions of the matrix where pores are largely spaced, which are constructed with both contour and hatch tracks. Second, they occur at about the same location across identical porous cells (Figures 5(a,b)), which were built using the same scanning strategy. Unlike lack-of-fusion defects that are often through-thickness, rounded pores are much smaller in size (Figure 6) and have a specific spatial distribution that corresponds to the laser contour trajectory (Figure 5(c)). These observations are consistent with what was reported for Ti6Al4V lattices produced by electron beam melting [57], and can be rationalized on account of the viscous forces trapping gas bubbles within the laser contour trajectory.

The influence of manufacturing defects on the elastic properties was not investigated in this study. It was examined in Ref. [34] for similar AlSi10Mg architectures, using image-based FE simulations combined with experiments. This work rather elucidated the role of manufacturing defects on the damage process. Notably, it was found that strain first concentrated around large matrix pores (see e.g. Figure 8(a)-Camera F for sample D20-w1), in agreement with earlier studies on both periodic lattices [29, 19, 59, 57] and random foams [60] produced by LPBF. By contrast, the pore geometric imperfections were found to exert no noticeable influence on damage initiation. For example, similar deformation features were measured across the two porous cells of sample D20-$w1$ (Figures 8(a)-(c)), despite the variations in pore ellipticity and/or size between both cells (with identical nominal geometry). This finding is consistent with what reported for other random porous media [33], and is of great practical importance. Notably, it indicates that structural disorder effectively mitigates the sensitivity to geometric imperfections. Reference [61] illustrates that point, highlighting the advantage offered by *disordered metamaterials* over periodic lattices. In unit-cell based structures, the imperfection sensitivity is instead exacerbated and causes for the sudden formation

of shear/collapse bands that eventually lead to failure [62, 33, 63]. This deformation mechanism is well documented for a large number of periodic lattices, including metallic structures fabricated by LPBF [57, 13, 19, 59, 18, 56, 64].

4.3. Mechanisms of tensile failure

The materials produced for this study contained two populations of micrometric voids, i.e., geometric and process-induced pores (Figure 5(d)). The first ones have larger cylindrical shapes and were designed, with the RSA algorithm, to achieve a 20% porosity. The second ones have smaller irregular geometry and do not exceed a few percent in volume (Section 3.3). Both types of pores are embedded within the aluminum matrix and are likely to promote the development of strained bands during tensile loading. It is well-known that in porous plastic solids, strains concentrate between large primary voids, and that small secondary voids (in the matrix material) accelerate the localization process [65]. This result was shown by the pioneering analyses of Needleman [66] and Tvergaard [67] using an idealized material model containing a square array of circular cylindrical voids, and agrees with the results presented in this study. The latter ones reveal that regions of intense deformation occurred between geometric pores and were heterogeneously distributed across the porous surface (Figures 7(a-d) and 8(a-d)). Only in the final stage of the fracture process, strains predominantly concentrated around the failure zone (Figures 7(e) and 8(e)). This deformation behavior is commonly observed in random porous media [54, 49, 33, 68] and is rationalized on the account of the geometric disorder, which caused a diffuse straining activity and prevented the sudden formation of a failure band.

To examine how the deformation accumulated in the present materials, the incremental strain maps for the two tested specimens are displayed in Figure 10. They measure the changes of local longitudinal strains in discrete macro-strain intervals $\Delta\langle E_{yy}\rangle$, and were computed for each cellular topology from the DIC-based displacement measurements corresponding to Figures 7 and 8. Figure 10 shows that the mechanisms of strain accumulation in both specimens were similar until departure from elasticity (Figure 10(a)), but differed remarkably with increasing plastic straining (Figures 10(b-f)). Two main differences are noted and are rationalized as follows. First, there is a tendency for more diffuse strain activity with decreasing pore aspect ratio. This trend is particularly evident at the beginning of the plastic

stage (Figures 10(b-d)), and is explained by the pore morphology. Prior FE studies showed that elliptical pores, with major axes aligned with the loading direction, lead to lower strain concentrations than their circular counterparts, and in turn delay the damage process [69, 70]. The data in Figure 4 corroborate these findings, reporting a higher rate of strain hardening in sample D20-w03 (with elliptical voids). The second difference is observed after the attainment of the peak stress. With increasing pore aspect ratio, the strains concentrated in a single band traversing groups of closely-spaced pores across the specimen's width (Figure 10(e,f)). This observation is consistent with prior analyses for similar random porous geometries [71, 72, 73], and is likely the consequence of the *cooperative* interaction between pores (both geometric and process-induced). Prior works show that if voids are spatially close or favorably oriented (with respect to the loading axis), plastic flow localizes into a band. This mechanism was first reported by Ohno and Hutchinson [74] and by Needleman and Tveergard [75], who examined respectively the effect of a non-uniform void distribution and of pore orientation on strain localization. The subject now comprises a large body of work, which is relevant to ductile fracture of metals [65].

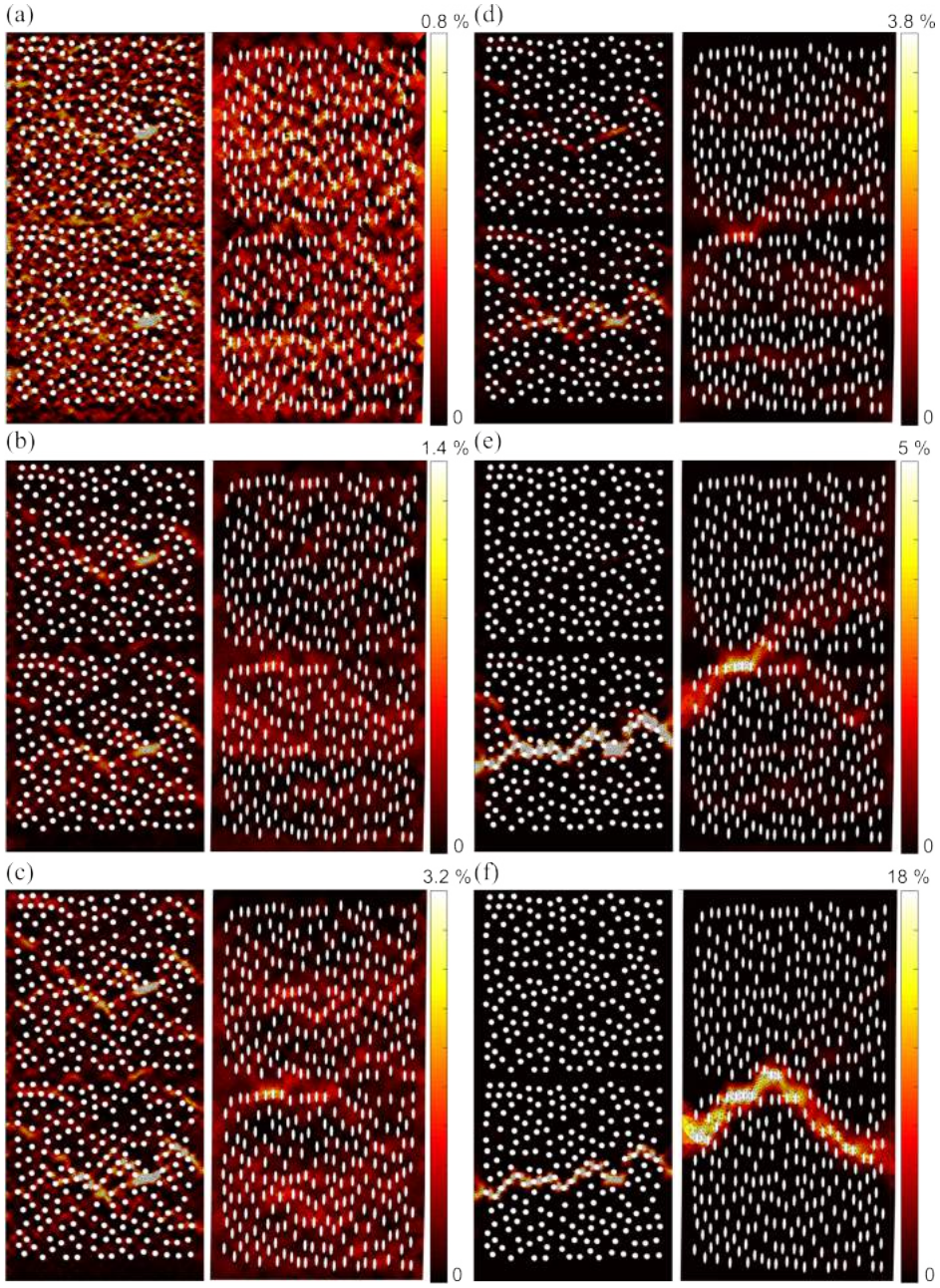

Figure 10: Incremental strain maps for specimens D20-w1 (left) and D20-w03 (right). They were computed from the displacement increments calculated via DIC from images collected by Cameras R and F, for specimen D20-w03 and D20-w1 respectively. Each reported map corresponds to a distinct macroscopic axial strain interval $\Delta\langle E_{yy}\rangle$, i.e., (a) $0\% - 0.16\%$, (b) $0.16\% - 0.27\%$, (c) $0.27\% - 0.65\%$, (d) $0.65\% - 0.77\%$, (e) $0.77\% - 1\%$, (f) $1\% - 1.2\%$. These strain levels are depicted with dotted lines in Figure 4 for each porous specimen.

528 The incremental strain maps (Figure 10) have important implications for the failure pro-

cess, as damage will likely initiate in regions of highly concentrated strains. Two distinct failure mechanisms are inferred from Figure 10 depending on the pore geometry. They are summarized as follows, and show several common features with the mechanisms of ductile fracture [65]. For sample D20-w03 with elliptical voids, failure was triggered by internal damage accumulation and resulted from the progressive propagation of a microcrack forming upon the first void coalescence. A distinct failure band only appeared at the very end of the fracture process (Figure 10(f) for sample D20-w03). Void coalescence occurred by internal necking of the matrix ligament between the pores, as suggested by the presence of dimples across the fractured surface of sample D20-w03 (Figure 9(c)). The presence of scattered strained sites (Figures 10(b-e)) also indicates that damage was diffuse over the porous surface, and likely competed with strain hardening. Figure 4(a-Camera R) corroborates these findings, showing a region of stress fluctuations around the peak load. Similar results were reported by Mangipudi and Onck for random foams under tension [54]. In the case of sample D20-w1 with circular voids, failure was instead triggered by plastic instability. The latter was distinguished by the formation of a localized strain band (Figures 10(d-e) for sample D20-w1), and was accompanied by elastic unloading in the outer material regions [76]. The DIC measurements provided this evidence, but are not shown here for the sake of brevity. Fracture was likely produced by void coalescence inside the band. Post-mortem tomographic images (Figure 5(a)) support this observation showing a *jagged* crack path linking groups of pores oriented at $\approx 45^{\circ}$ with respect to the macroscopic principal stress axis. Coalescence was induced by a shearing process. This type of void coalescence mechanism, known as *void sheeting*, has been observed experimentally first by Cox and Low [77] and by several other authors since then [78, 79, 80, 81]. It is known to be favored by the presence of secondary voids and is accompanied with large pore shape changes [65]. Tomographic observations (Figure 5) corroborate these findings, showing evidence of large pore distortions upon coalescence (Figure 5(a)) as well as the presence of smaller process-induced voids (Figure 5(c,d)).

4.4. Comparison with McClintock's micromechanical model

Plastic deformation is known to affect the rate at which pores grow in tension [65]. In this study, the measured strain fields were highly heterogeneous (Figures 7 and 8), and exhibited distinct accumulation mechanisms with varying pore geometry (Figure 10). It is therefore

reasonable to expect that the rate of void growth varied within the same specimen, and also between the two cellular topologies. Figure 11, which confirms this statement, reports for all geometric voids within each specimen, the pore true strain at discrete instants of the deformation history. This quantity is defined as the variation of the pore area over time (i.e., $\ln(A/A_0)$, where A and A_0 denote respectively the current and initial pore areas), and was computed, for each pore, from its major and minor axes. The actual pore geometry was in turn quantified after interpolation (via a conic function) of the nodal pore coordinates, measured via FE-based DIC using meshes consistent with the porous architecture (Section 2.4). Figure 11 highlights two major trends. First, it shows that void deformation was highly heterogeneous in both specimens and was higher for pores within areas of intense strain (Figures 11(a-d)). This last observation could be made by comparing pairwise Figures 11(a-d) with Figures 10(a-d) for specimen D20-w1 with circular voids, and was in turn expected as pores grow aided by plasticity [66, 82, 65]. Second, Figure 11 reveals that, upon macroscopic instability, void deformation was entirely localized inside the shear band (see Figures 11(e-f) for sample D20-w1 with circular pores). Pores in this band were no longer, even approximately, circular (Figures 11(e-f)) as a result of *void sheeting* [78, 79, 80, 81].

To quantify the rate of void growth during tensile straining, the change of the pore mean radius, $\ln(R_m/R_{m0})$, with the applied macroscopic deformation, $\langle E_{yy} \rangle$, is shown in Figures 12(a,b) for all geometric pores in each tensile sample. This geometric parameter was chosen for convenience as its initial value (i.e., R_{m0}) was similar for both cellular topologies (Table 1). For the sake of comparison, measurements corresponding to different geometric pores across each specimen are reported using different line colors. Collectively, the data in Figures 12(a,b) reflect the trends observed in Figure 11, indicating highly heterogeneous void growth across each specimen. Moreover, they show that the rate of void growth increased significantly upon the attainment of the maximum stress, for the pores in the fracture path. The latter ones are indicated in the inset figure for each cellular topology, and were found to grow significantly faster than all other pores in the specimen (Figures 12(a,b)). In particular, a higher void growth rate was measured in specimen D20-w1 with circular pores. Similar results were reported by Dubensky and Koss [71] and were rationalized on account of the cooperative interaction of the pores within the shear band, which eventually coalesce by a *void-sheeting* mechanism.

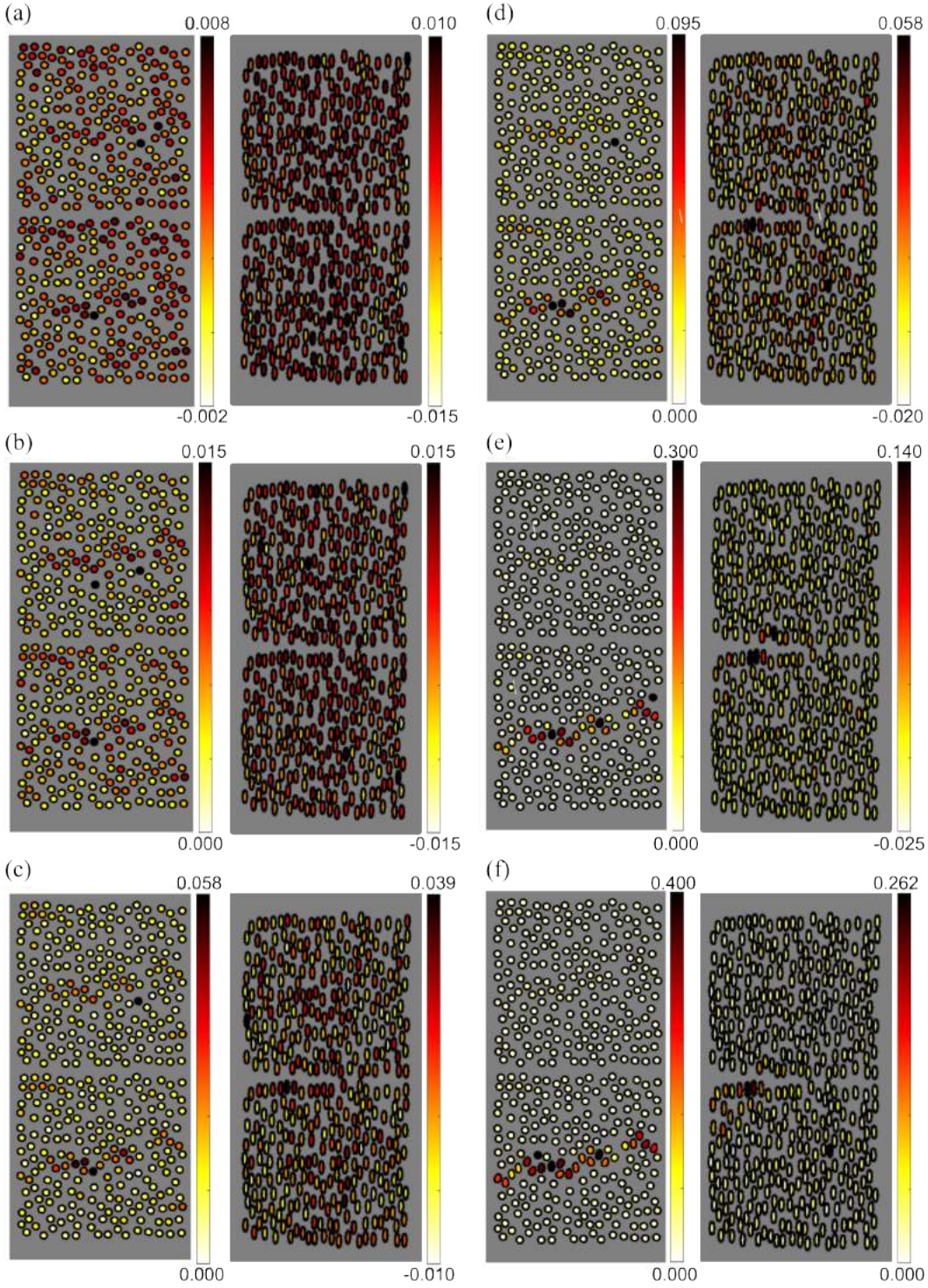

Figure 11: True pore strain maps (as determined from the pore area, i.e. $\ln(A/A_0)$) for specimens (left) D20-w1 and (right) D20-w03 at discrete points of the deformation history. Data for specimens D20-w1 and D20-w03 were computed from Camera F and Camera R, respectively. The macroscopic longitudinal strain $\langle E_{yy} \rangle$ was equal to: (a) 0.16%, (b) 0.27%, (c) 0.65%, (d) 0.77%, (e) 1% and (f) 1.2%. These levels are depicted with dotted lines in Figure 4 for each porous specimen.

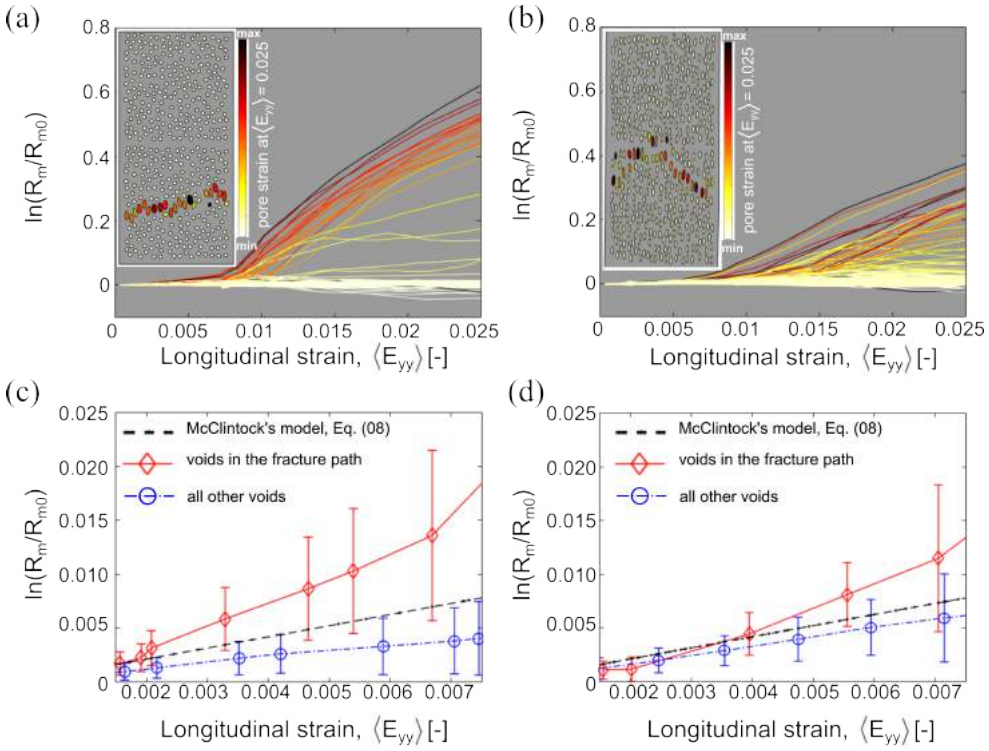

Figure 12: (a)-(b) Growth of the mean pore radius $\ln(R_m/R_{m0})$ as a function of the macroscopic strain $\langle \mathrm{E}_{yy} \rangle$ in specimens (a) D20-w1 and (b) D20-w03. Data for specimens D20-w1 and D20-w03 were computed from Camera F and Camera R, respectively. Different line colors indicate different pores across each specimen. The latter ones are shown in their deformed state in the inset of each figure at $\langle \mathrm{E}_{yy} \rangle = 2.5\%$. (c)-(d) Comparison between the McClintock's model predictions (Equation 8) and the experimental data for specimens (c) D20-w1 and (d) D20-w03. For each cellular topology, the average value of the mean pore radius growth is reported for two sets of pores (i.e., for the pores inside and outside the fracture band). Error bars represent the measurements standard deviation.

The effect of void interaction is not taken into account by the well-known McClintock void growth model [30]. The latter was formulated by solving the generalized plane-strain deformation problem of an isolated cylindrical hole in an infinite plastic medium. McClintock postulates that the pore mean radius (i.e., $\ln(R_m/R_{m0})$) increases with increasing equivalent applied strain (i.e., $\bar{\epsilon}$) and is given by (see Equation (23) in Ref. [30])

$$\ln\left(\frac{R_m}{R_{m0}}\right) = \frac{\sqrt{3}\bar{\epsilon}}{2\,(1-n)} \sinh\left(\frac{\sqrt{3}\,(1-n)}{2}\frac{\sigma_a+\sigma_b}{\bar{\sigma}}\right) + \frac{\epsilon_a+\epsilon_b}{2}, \tag{7}$$

where n and $\bar{\sigma}$ denote the strain-hardening coefficient and the equivalent macroscopic stress, respectively. The applied stresses σ_a and σ_b are those in the major and minor pore axes

(principal) directions, and ϵ_a and ϵ_b the corresponding strains. For an elliptical hole deformed in tension under plane strain conditions (i.e., $\epsilon_a = -\epsilon_b$ and the out-of-plane normal stress is $\sigma_z = (\sigma_a + \sigma_b)/2$ [30]), Equation (7) becomes

$$\ln\left(\frac{R_m}{R_{m0}}\right) = \frac{\langle E_{yy}\rangle}{(1-n)}\sinh(1-n)\,. \tag{8}$$

The comparison between the predictions of McClintock's model (Equation (8) with $n = 0.5$, where the latter is given in Ref. [49] for an Al-matrix) and the experimental data is displayed in Figures 12(c,d) for applied macroscopic deformations up to $\langle \mathrm{E}_{yy}\rangle = 0.75\%$ (i.e. c.a. up to $\approx \epsilon_{UTS}$, see Table 3.2). To make the comparison easier, the average value of the mean radius growth $\ln(R_m/R_{m0})$ is reported for each cellular topology. This quantity was computed from the measurements reported in Figures 12(a,b) for two sets of pores (i.e., for the voids inside and outside the fracture path, see insets of Figures 12(a,b)). For each set of experimental data, the standard deviations at discrete values of the applied axial strain are also reported. Figure 12(c,d) first shows that the growth of the mean pore radius was proportional to the applied macroscopic strain, and was lower for the holes outside the fracture band (compare the blue and red lines across Figure 12(c,d)). These findings are consistent with the results of prior studies [83, 84, 71], and agree well with McClintock's analysis [30]. For this set of pores, the comparison between the predictions of Equation (8) and the experimental data is particularly satisfactory for specimen D20-w03 with elliptical holes (compare black and blue lines in Figure 12(d)), thereby confirming that void interactions were small outside the failure band. Conversely, McClintock's model underestimated the measured data for the void growth inside the fracture path (see black and red lines in Figure 12(c,d)). This discrepancy is due to the model assumptions (neglecting void interaction [77]) and is more pronounced for specimen D20-w1 with circular voids. For the latter, void interactions occurred since the very early stages of deformation (Figure 8) and concentrated predominantly within the shear band (Figure 11).

The presence of a large irregular defect within the failure band of specimen D20-w1 (highlighted with a red line in Figure 5(a)) likely exacerbated the effects of void interaction, promoting early plastic flow localization. This observation is consistent with prior studies on the effect of void cluster [74, 82, 85], and is likely the cause of the higher discrepancy with McClintocks' model predictions (Figure 12(c)). Tomographic reconstructions in Figure 5(a)

also corroborate this statement, providing experimental evidence of the interaction between geometric voids and matrix defects. Notably, they showed that the crack-tip of the defect, highlighted with a red line in Figure 5(a)-bottom cell, coalesced with its closest geometric pores along the direction of the tensile axis.

Closing this section, it is also worth emphasizing some of the main limitations of micromechanical models based on periodic arrays of voids. Since the seminal works of Needleman [66] and Tveergard [67], unit cell models have been successful in rationalizing salient features of ductile fracture processes [86]). While models of this type will likely remain very useful tools for investigation purposes, they fail to capture most of the findings produced in this study. The latter ones notably included the effects of non-uniform pore distributions on strain heterogeneities and localization (Figures 7, 8 and 10). This point was raised by several authors [87, 76] and, in turn, opens up novel perspectives for this class of random metamaterials, which may prove attractive *porous systems* for the study of ductile fracture at the mesoscale.

5. Conclusion

This work investigated experimentally the tensile response of metallic cellular metamaterials that contained randomly-dispersed cylindrical pores at $\approx 20\%$ in vol. fraction. Their porous architecture was generated numerically via a random sequential absorption algorithm, and was fabricated by LPBF from AlSi10Mg powders.

Using FE-based DIC (where the pore meshes were consistent with the cellular topology), the mesoscale deformation mechanisms were quantified for this class of disordered porous materials. Notably, it was shown that they are distinguished by non-uniform strain distributions and are triggered by the interaction between geometric pores. The latter was, in turn, promoted by the presence of smaller pores and lack-of-fusion defects within the AlSi10Mg matrix, as revealed by X-Ray tomography. Defects of this type resulted from the manufacturing process and are typically observed in parts produced by LPBF.

Equally important, the results of this study showed that the mechanisms of strain concentration varied with the pore geometry and exhibited several common features with the ductile failure mechanisms of metals, albeit at the mesoscale. For example, with increasing pore aspect ratio, fracture occurred by *void-sheet* coalescence and resulted from macroscopic

plastic instability. Conversely, more elongated elliptical voids caused diffuse strained areas and delayed the fracture process. Moreover, strain localization affected the void growth rate. It was shown that the pores in the failure band grew much faster than all other pores and that McClintock's model could not predict the experimental data for the average void growth rate in the fracture band.

The results of this study have important implications for micromechanical models used to study void growth and coalescence, and in turn open up novel perspectives for this class of random porous metamaterials as convenient model systems for the study of ductile fracture of metallic alloys.

6. Acknowledgments

L.S. was supported by the Erasmus+ mobility program and by Idex Paris-Saclay via the *Institut Intégratif des Matériaux* of the Université Paris-Saclay. This work was partially supported by the French "Agence Nationale de la Recherche" through the "Investissements d'avenir" program (ANR-10-EQPX-37MATMECAGrant), and by the CNRS Cellule Energie via the program PEPS Energie 2021. The authors would also like to thank Dr. P. Peyre and Mrs. C. Dupuy at PIMM/ENSAM Paris for both the LPBF fabrication of the specimens and the insightful discussions on the origin of the manufacturing defects in the parts fabricated for this study. Last, the help of M. Bonnet for the SEM fractographic analysis and of L. Hachemi for the metallographic preparation is also greatly acknowledged.

7. Appendix

The backtracking procedure was instrumental to ensure that the DIC meshes were consistent with the actual pore distribution. In this section, the backtracking technique, allowing the pores to be correctly positioned on the adapted mesh for the two porous specimens is detailed. The technique uses a correlation algorithm that instead of correlating two consecutive images, as in classical DIC, registers a real and an ideal image [40]. A coarse auxiliary mesh was used to measure the displacement field enabling for the best possible match. To evaluate the quality of the converged solution, the gray level residuals (Section 2.4.1) were analyzed. Grayish zones correspond to good correlation, whereas black and white zones highlight areas

683 with manufacturing defects. For instance, the white zones are associated with lack-of-fusion
684 defects that are present in the real volume section but not in the nominal image.

685 *From mask to mesh*

686 This first approach was applied to images acquired by Camera F. In that case, the ideal
687 image consisted in an indexed mask numerically reconstructed starting from the nominal
688 parameters of the porous matrix (i.e., pore positions, orientation and dimensions). A fine
689 triangular mesh was then created on the material indexed zone of the image via the open-
690 source software Gmsh [88]. In Figure 13(a), an example is shown for the mesh of specimen
691 D20-w03 for Camera F. The numerical mask was correlated to the real image (first frame
692 captured during testing) through a correlation algorithm thanks to a coarse auxiliary mesh
693 (Figure 13(b)). The coarse mesh assesses the displacement field the ideal mesh should undergo
694 to adapt to the real image. Thanks to an interpolation between the coarse and refined meshes,
695 it is possible to move back each node of the model-based mesh. In Figure 13(b), the coarse
696 mesh is depicted in orange. The correlation residuals after backtracking prove that the pores
697 were properly repositioned (Figure 13(c)).

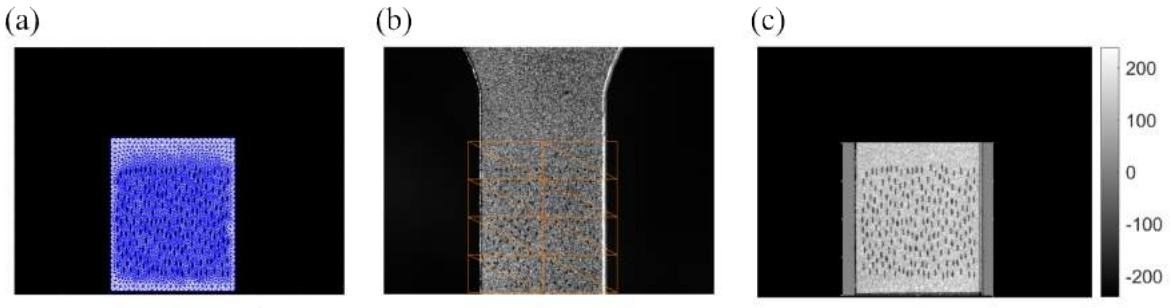

Figure 13: (a) Gmsh generated mesh to be backtracked and superimposed onto the nominal mask. (b) Reference image of Camera F for specimen D20-w03 with the coarse backtracking mesh depicted in orange. (c) Gray level residual map to backtrack the mesh of specimen D20-w03 and Camera F showing that the backtracking procedure was successful.

698 *From mesh to mask*

699 This technique was applied to the images acquired by Camera R. Its lower resolution
700 did not allow the numerically generated pores to be correlated to those present in the real
701 image. The correlation was made possible by the curved edges, still visible in Camera R

images, thanks to the lower zoom factor. In the absence of a numerical file containing all positions of pores and edge lines, the numerical mask was built starting from the mesh of the dogbone sample. A 2D .stp file of the full dogbone specimen (not only the porous part) was available. A triangular fine mesh, displayed in Figure 14(a), was directly obtained on the solid part by using the Abaqus interface [89]. The meshed specimen was then manually prepositioned on the reference image and then backtracked. In that case, the indexed mask was built starting from the Abaqus mesh, then imported in the DIC code, and the node to pixel projector was used to determine which pixels belonged to the mesh. Once the mask in Figure 14(b) was obtained, it was correlated with the reference image thanks to the coarse auxiliary mesh represented in Figure 14(c). The displacement field obtained on the coarse mesh was interpolated on the deformed mesh, thus obtaining the backtracked mesh shown in Figure 15(b).

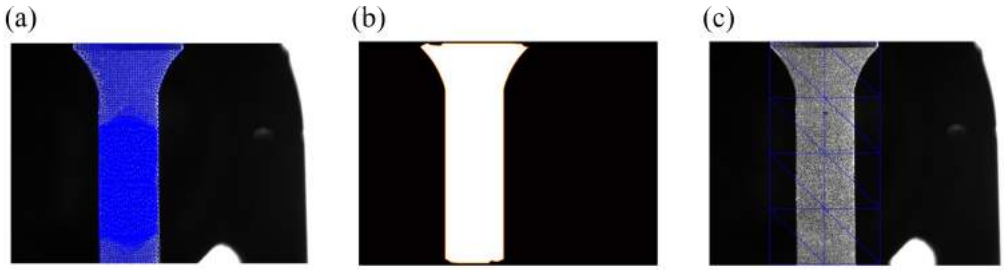

Figure 14: (a) Prepositioned mesh generated on the dogbone CAD model laid over the reference image. (b) Reconstructed mask, and (c) auxiliary (blue) mesh in the reference image

The backtracked meshes for the two porous specimens and both cameras are shown in Figure 15. They were utilized to report DIC analyses at the mescoscale level.

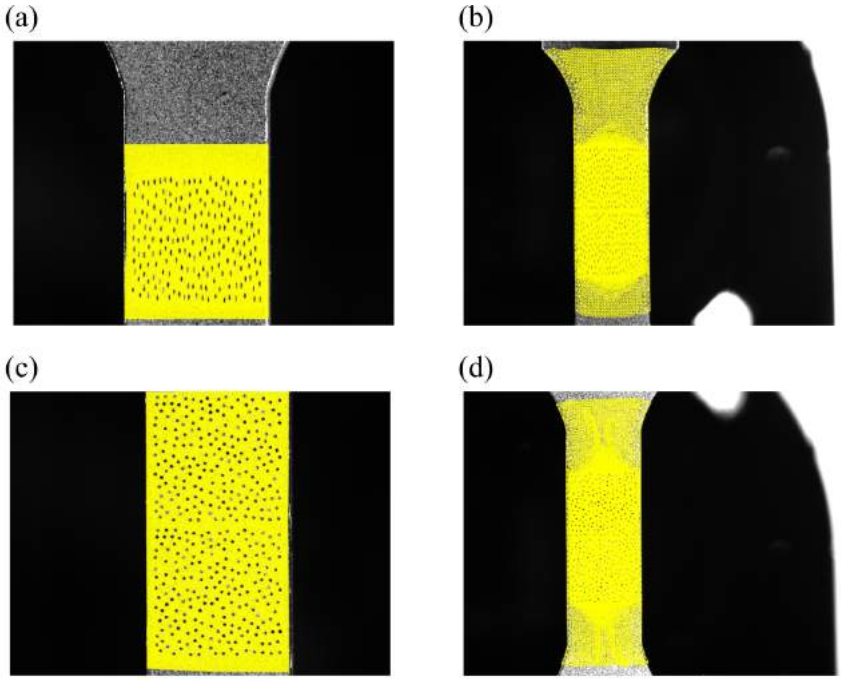

Figure 15: Backtracked meshes of sample D20-w03 for Cameras (a) F and (b) R acquisitions, and specimen D20-w1 for Cameras (c) F and (d) R acquisitions, respectively

References

[1] J. Banhart, Manufacture, characterisation and application of cellular metals and metal foams, Progress in materials science 46 (6) (2001) 559–632.

[2] N. A. Fleck, V. S. Deshpande, M. F. Ashby, Micro-architectured materials: past, present and future, Proceedings of the Royal Society A: Mathematical, Physical and Engineering Sciences 466 (2121) (2010) 2495–2516.

[3] T. A. Schaedler, W. B. Carter, Architected cellular materials, Annual Review of Materials Research 46 (2016) 187–210.

[4] T. A. Schaedler, A. J. Jacobsen, A. Torrents, A. E. Sorensen, J. Lian, J. R. Greer, L. Valdevit, W. B. Carter, Ultralight metallic microlattices, Science 334 (6058) (2011) 962–965.

[5] J. H. Pikul, H. Gang Zhang, J. Cho, P. V. Braun, W. P. King, High-power lithium ion microbatteries from interdigitated three-dimensional bicontinuous nanoporous electrodes, Nature communications 4 (1) (2013) 1732.

[6] B. Blakey-Milner, P. Gradl, G. Snedden, M. Brooks, J. Pitot, E. Lopez, M. Leary, F. Berto, A. Du Plessis, Metal additive manufacturing in aerospace: A review, Materials & Design 209 (2021) 110008.

[7] A. A. Zadpoor, Additively manufactured porous metallic biomaterials, Journal of Materials Chemistry B 7 (26) (2019) 4088–4117.

[8] T. Tancogne-Dejean, A. B. Spierings, D. Mohr, Additively-manufactured metallic micro-lattice materials for high specific energy absorption under static and dynamic loading, Acta Materialia 116 (2016) 14–28.

[9] J. Y. Ho, K. C. Leong, T. N. Wong, Additively-manufactured metallic porous lattice heat exchangers for air-side heat transfer enhancement, International Journal of Heat and Mass Transfer 150 (2020) 119262.

[10] V. Egorov, C. O'Dwyer, Architected porous metals in electrochemical energy storage, Current Opinion in Electrochemistry 21 (2020) 201–208.

[11] A. Du Plessis, N. Razavi, M. Benedetti, S. Murchio, M. Leary, M. Watson, D. Bhate, F. Berto, Properties and applications of additively manufactured metallic cellular materials: A review, Progress in Materials Science 125 (2022) 100918.

[12] H. N. Wadley, Multifunctional periodic cellular metals, Philosophical Transactions of the Royal Society A: Mathematical, Physical and Engineering Sciences 364 (1838) (2006) 31–68.

[13] L. Liu, P. Kamm, F. García-Moreno, J. Banhart, D. Pasini, Elastic and failure response of imperfect three-dimensional metallic lattices: the role of geometric defects induced by selective laser melting, Journal of the Mechanics and Physics of Solids 107 (2017) 160–184.

[14] M. Araya, M. Jaskari, T. Rautio, T. Guillén, A. Järvenpää, Assessing the compressive and tensile properties of tpms-gyroid and stochastic ti64 lattice structures: A study on laser powder bed fusion manufacturing for biomedical implants, Journal of Science: Advanced Materials and Devices (2023) 100663.

[15] V. S. Deshpande, N. A. Fleck, M. F. Ashby, Effective properties of the octet-truss lattice material, Journal of the Mechanics and Physics of Solids 49 (8) (2001) 1747–1769.

[16] V. Deshpande, M. Ashby, N. Fleck, Foam topology: bending versus stretching dominated architectures, Acta materialia 49 (6) (2001) 1035–1040.

[17] P. Köhnen, C. Haase, J. Bültmann, S. Ziegler, J. H. Schleifenbaum, W. Bleck, Mechanical properties and deformation behavior of additively manufactured lattice structures of stainless steel, Materials & Design 145 (2018) 205–217.

[18] R. Goodall, E. Hernandez-Nava, S. N. Jenkins, L. Sinclair, E. Tyrwhitt-Jones, M. A. Khodadadi, D. H. Ip, H. Ghadbeigi, The effects of defects and damage in the mechanical behavior of ti6al4v lattices, Frontiers in Materials 6 (2019) 117.

[19] Y. Amani, S. Dancette, P. Delroisse, A. Simar, E. Maire, Compression behavior of lattice structures produced by selective laser melting: X-ray tomography based experimental and finite element approaches, Acta Materialia 159 (2018) 395–407.

[20] M. R. O'Masta, L. Dong, L. St-Pierre, H. Wadley, V. S. Deshpande, The fracture toughness of octet-truss lattices, Journal of the Mechanics and Physics of Solids 98 (2017) 271–289.

[21] M. Valmalle, A. Vintache, B. Smaniotto, F. Gutmann, M. Spagnuolo, A. Ciallella, F. Hild, Local–global dvc analyses confirm theoretical predictions for deformation and damage onset in torsion of pantographic metamaterial, Mechanics of Materials 172 (2022) 104379.

[22] X. Geng, Y. Lu, C. Liu, W. Li, Z. Yue, Fracture characteristic analysis of cellular lattice structures under tensile load, International Journal of Solids and Structures 163 (2019) 170–177.

[23] S. Daynes, J. Lifton, W. F. Lu, J. Wei, S. Feih, Fracture toughness characteristics of additively manufactured ti–6al–4v lattices, European Journal of Mechanics-A/Solids 86 (2021) 104170.

[24] H. Alsalla, L. Hao, C. Smith, Fracture toughness and tensile strength of 316l stainless steel cellular lattice structures manufactured using the selective laser melting technique, Materials Science and Engineering: A 669 (2016) 1–6.

[25] M. Gavazzoni, M. Pisati, S. Beretta, S. Foletti, Multiaxial static strength of a 3d printed metallic lattice structure exhibiting brittle behavior, Fatigue & Fracture of Engineering Materials & Structures 44 (12) (2021) 3499–3516.

[26] M. Benedetti, A. Du Plessis, R. Ritchie, M. Dallago, S. M. J. Razavi, F. Berto, Architected cellular materials: A review on their mechanical properties towards fatigue-tolerant design and fabrication, Materials Science and Engineering: R: Reports 144 (2021) 100606.

[27] L. Boniotti, S. Beretta, L. Patriarca, L. Rigoni, S. Foletti, Experimental and numerical investigation on compressive fatigue strength of lattice structures of alsi7mg manufactured by slm, International Journal of Fatigue 128 (2019) 105181.

[28] P. E. Seiler, K. Li, V. S. Deshpande, N. A. Fleck, The influence of strut waviness on the tensile response of lattice materials, Journal of Applied Mechanics 88 (3) (2021) 031011.

[29] A. Du Plessis, I. Yadroitsava, I. Yadroitsev, Effects of defects on mechanical properties in metal additive manufacturing: A review focusing on x-ray tomography insights, Materials & Design 187 (2020) 108385.

[30] F. A. McClintock, A criterion for ductile fracture by the growth of holes (1968).

[31] O. Zerhouni, M. Tarantino, K. Danas, Numerically-aided 3d printed random isotropic porous materials approaching the hashin-shtrikman bounds, Composites Part B: Engineering 156 (2019) 344–354.

[32] M. Tarantino, O. Zerhouni, K. Danas, Random 3d-printed isotropic composites with high volume fraction of pore-like polydisperse inclusions and near-optimal elastic stiffness, Acta materialia 175 (2019) 331–340.

[33] Z. Hooshmand-Ahoor, M. Tarantino, K. Danas, Mechanically-grown morphogenesis of voronoi-type materials: Computer design, 3d-printing and experiments, Mechanics of Materials 173 (2022) 104432.

[34] S. Leonardi, C. Dupuy, P. Peyre, A. Helbert, M. Tarantino, Architected metallic cellular materials with random pore features: computer design, lpbf fabrication and mechanical properties, Procedia Structural Integrity 53 (2024) 327–337.

[35] O. Zerhouni, M.-G. Tarantino, K. Danas, F. Hong, Influence of the internal geometry on the elastic properties of materials using 3d printing of computer-generated random microstructures, in: SEG International Exposition and Annual Meeting, SEG, 2018, pp. SEG–2018.

[36] N. T. Aboulkhair, I. Maskery, C. Tuck, I. Ashcroft, N. M. Everitt, The microstructure and mechanical properties of selectively laser melted alsi10mg: The effect of a conventional t6-like heat treatment, Materials Science and Engineering: A 667 (2016) 139–146.

[37] W. Li, S. Li, J. Liu, A. Zhang, Y. Zhou, Q. Wei, C. Yan, Y. Shi, Effect of heat treatment on alsi10mg alloy fabricated by selective laser melting: Microstructure evolution, mechanical properties and fracture mechanism, Materials Science and Engineering: A 663 (2016) 116–125.

[38] S. Bagherifard, N. Beretta, S. Monti, M. Riccio, M. Bandini, M. Guagliano, On the fatigue strength enhancement of additive manufactured alsi10mg parts by mechanical and thermal post-processing, Materials & Design 145 (2018) 28–41.

[39] Z. Tomičević, F. Hild, S. Roux, Mechanics-aided digital image correlation, J. Strain Analysis 48 (2013) 330–343.

[40] F. Hild, A. Misra, F. dell'Isola, Multiscale DIC Applied to Pantographic Structures, Experimental Mechanics (2021) 61:431–443.

[41] D. Claire, F. Hild, S. Roux, A finite element formulation to identify damage fields: The equilibrium gap method, Int. J. Num. Meth. Engng. 61 (2) (2004) 189–208.

[42] H. Leclerc, J. Neggers, F. Mathieu, F. Hild, S. Roux, Correli 3.0, IDDN.FR.001.520008.000.S.P.2015.000.31500, Agence pour la Protection des Programmes, Paris (France) (2015).

[43] W. Liu, C. Chen, S. Shuai, R. Zhao, L. Liu, X. Wang, T. Hu, W. Xuan, C. Li, J. Yu, et al., Study of pore defect and mechanical properties in selective laser melted ti6al4v alloy based on x-ray computed tomography, Materials Science and Engineering: A 797 (2020) 139981.

[44] L. Zhao, L. Song, J. G. S. Macías, Y. Zhu, M. Huang, A. Simar, Z. Li, Review on the correlation between microstructure and mechanical performance for laser powder bed fusion alsi10mg, Additive Manufacturing 56 (2022) 102914.

[45] M. Tarantino, A. Mortensen, On the bulk compressibility of close-packed particles and their composites, Composites Part A: Applied Science and Manufacturing 161 (2022) 107106.

[46] K. Anoukou, R. Brenner, F. Hong, M. Pellerin, K. Danas, Random distribution of polydisperse ellipsoidal inclusions and homogenization estimates for porous elastic materials, Computers & Structures 210 (2018) 87–101.

[47] M. Masmoudi, W. Kaddouri, T. Kanit, S. Madani, S. Ramtani, A. Imad, Modeling of the effect of the void shape on effective ultimate tensile strength of porous materials: Nu-

merical homogenization versus experimental results, International Journal of Mechanical Sciences 130 (2017) 497–507.

[48] S. Hyun, K. Murakami, H. Nakajima, Anisotropic mechanical properties of porous copper fabricated by unidirectional solidification, Materials Science and Engineering: A 299 (1-2) (2001) 241–248.

[49] C. Motz, R. Pippan, Deformation behaviour of closed-cell aluminium foams in tension, Acta Materialia 49 (13) (2001) 2463–2470.

[50] E. Amsterdam, P. Onck, J. T. M. De Hosson, Fracture and microstructure of open cell aluminum foam, Journal of materials science 40 (2005) 5813–5819.

[51] C. San Marchi, J.-F. Despois, A. Mortensen, Uniaxial deformation of open-cell aluminum foam: the role of internal damage, Acta materialia 52 (10) (2004) 2895–2902.

[52] J.-F. Despois, R. Mueller, A. Mortensen, Uniaxial deformation of microcellular metals, Acta materialia 54 (16) (2006) 4129–4142.

[53] W. Ronan, V. S. Deshpande, N. A. Fleck, The tensile ductility of cellular solids: the role of imperfections, International Journal of Solids and Structures 102 (2016) 200–213.

[54] K. R. Mangipudi, P. Onck, Multiscale modelling of damage and failure in two-dimensional metallic foams, Journal of the Mechanics and Physics of Solids 59 (7) (2011) 1437–1461.

[55] K. Mangipudi, P. Onck, Tensile failure of two-dimensional quasi-brittle foams, International Journal of Solids and Structures 49 (19-20) (2012) 2823–2829.

[56] L. Xiao, S. Li, W. Song, X. Xu, S. Gao, Process-induced geometric defect sensitivity of ti–6al–4v lattice structures with different mesoscopic topologies fabricated by electron beam melting, Materials Science and Engineering: A 778 (2020) 139092.

[57] E. Hernández-Nava, C. Smith, F. Derguti, S. Tammas-Williams, F. Léonard, P. J. Withers, I. Todd, R. Goodall, The effect of defects on the mechanical response of ti-6al-4v cubic lattice structures fabricated by electron beam melting, Acta Materialia 108 (2016) 279–292.

[58] X. Chen, W. Liao, H. Wei, Z. Zhu, T. Yang, C. Zhang, T. Liu, Formation mechanisms and control strategies of metallurgical defects and microstructures during laser powder bed fusion of alsi10mg lattice structures, Journal of Materials Research and Technology 28 (2024) 139–153.

[59] M. Dallago, B. Winiarski, F. Zanini, S. Carmignato, M. Benedetti, On the effect of geometrical imperfections and defects on the fatigue strength of cellular lattice structures additively manufactured via selective laser melting, International Journal of Fatigue 124 (2019) 348–360.

[60] E. Hernández-Nava, C. Smith, F. Derguti, S. Tammas-Williams, F. Léonard, P. J. Withers, I. Todd, R. Goodall, The effect of density and feature size on mechanical properties of isostructural metallic foams produced by additive manufacturing, Acta Materialia 85 (2015) 387–395.

[61] M. Zaiser, S. Zapperi, Disordered mechanical metamaterials, Nature Reviews Physics 5 (11) (2023) 679–688.

[62] M.-G. Tarantino, K. Danas, Programmable higher-order euler buckling modes in hierarchical beams, International Journal of Solids and Structures 167 (2019) 170–183.

[63] F. Albertini, M. G. Tarantino, L. Daniel, Mechanical behavior of embedded bistable dome shell with tunable energy barrier asymmetry, International Journal of Mechanical Sciences 263 (2024) 108762.

[64] L. Zhang, J. Lifton, Z. Hu, R. Hong, S. Feih, Influence of geometric defects on the compression behaviour of thin shell lattices fabricated by micro laser powder bed fusion, Additive Manufacturing 58 (2022) 103038.

[65] A. Pineau, A. A. Benzerga, T. Pardoen, Failure of metals i: Brittle and ductile fracture, Acta Materialia 107 (2016) 424–483.

[66] A. Needleman, Void growth in an elastic-plastic medium (1972).

[67] V. Tvergaard, On localization in ductile materials containing spherical voids, International Journal of fracture 18 (1982) 237–252.

[68] Z. Hooshmand-Ahoor, H. Luo, K. Danas, M-voronoi and other random open and closed-cell elasto-plastic cellular materials: Geometry generation and numerical study at small and large strains, International Journal of Solids and Structures (2024) 112680.

[69] H. Li, S. M. Oppenheimer, S. I. Stupp, D. C. Dunand, L. C. Brinson, Effects of pore morphology and bone ingrowth on mechanical properties of microporous titanium as an orthopaedic implant material, Materials Transactions 45 (4) (2004) 1124–1131.

[70] N. Winter, M. Becton, L. Zhang, X. Wang, Effects of pore design on mechanical properties of nanoporous silicon, Acta Materialia 124 (2017) 127–136.

[71] E. Dubensky, D. A. Koss, Void/pore distributions and ductile fracture, Metallurgical Transactions A 18 (1987) 1887–1895.

[72] P. Magnusen, E. Dubensky, D. Koss, The effect of void arrays on void linking during ductile fracture, Acta Metallurgica 36 (6) (1988) 1503–1509.

[73] A. Al-Ostaz, I. Jasiuk, Crack initiation and propagation in materials with randomly distributed holes, Engineering Fracture Mechanics 58 (5-6) (1997) 395–420.

[74] N. Ohno, J. Hutchinson, Plastic flow localization due to non-uniform void distribution, Journal of the Mechanics and Physics of Solids 32 (1) (1984) 63–85.

[75] V. Tvergaard, A. Needleman, Nonlocal effects on localization in a void-sheet, International Journal of Solids and Structures 34 (18) (1997) 2221–2238.

[76] C. Tekoğlu, J. Hutchinson, T. Pardoen, On localization and void coalescence as a precursor to ductile fracture, Philosophical Transactions of the Royal Society A: Mathematical, Physical and Engineering Sciences 373 (2038) (2015) 20140121.

[77] T. Cox, J. R. Low, An investigation of the plastic fracture of aisi 4340 and 18 nickel-200 grade maraging steels, Metallurgical and Materials Transactions B 5 (1974) 1457–1470.

[78] A. Weck, D. Wilkinson, Experimental investigation of void coalescence in metallic sheets containing laser drilled holes, Acta Materialia 56 (8) (2008) 1774–1784.

[79] T. F. Morgeneyer, T. Taillandier-Thomas, L. Helfen, T. Baumbach, I. Sinclair, S. Roux, F. Hild, In situ 3-d observation of early strain localization during failure of thin al alloy (2198) sheet, Acta Materialia 69 (2014) 78–91.

[80] A. Buljac, L. Helfen, F. Hild, T. F. Morgeneyer, Effect of void arrangement on ductile damage mechanisms in nodular graphite cast iron: In situ 3d measurements, Engineering Fracture Mechanics 192 (2018) 242–261.

[81] F. Hannard, A. Simar, E. Maire, T. Pardoen, Quantitative assessment of the impact of second phase particle arrangement on damage and fracture anisotropy, Acta materialia 148 (2018) 456–466.

[82] J. Bandstra, D. Koss, On the influence of void clusters on void growth and coalescence during ductile fracture, Acta Materialia 56 (16) (2008) 4429–4439.

[83] E. Maire, C. Bordreuil, L. Babout, J.-C. Boyer, Damage initiation and growth in metals. comparison between modelling and tomography experiments, Journal of the Mechanics and Physics of Solids 53 (11) (2005) 2411–2434.

[84] A. Hosokawa, D. S. Wilkinson, J. Kang, E. Maire, Onset of void coalescence in uniaxial tension studied by continuous x-ray tomography, Acta Materialia 61 (4) (2013) 1021–1036.

[85] M. Worswick, Z. Chen, A. Pilkey, D. Lloyd, S. Court, Damage characterization and damage percolation modelling in aluminum alloy sheet, Acta Materialia 49 (14) (2001) 2791–2803.

[86] T. Pardoen, J. Hutchinson, An extended model for void growth and coalescence, Journal of the Mechanics and Physics of Solids 48 (12) (2000) 2467–2512.

[87] R. Becker, R. Smelser, Simulation of strain localization and fracture between holes in an aluminum sheet, Journal of the Mechanics and Physics of Solids 42 (5) (1994) 773–796.

[88] C. Geuzaine, J.-F. Remacle, Gmsh: A 3D finite element mesh generator with built-in pre-and post-processing facilities, International Journal for Numerical Methods in Engineering 79 (11) (2009) 1309–1331.

[89] Dassault Systèmes Simulia Corp., Providence, RI, USA., Abaqus 6.14 Documentation (2014).